APPLICATION OF NEWBORN JAUNDICE DETERMINATION AND DESIGN OF A NONINVASIVE BILIRUBINOMETER

by

Yunus Karamavuş

B.S. in Electronics Engineering, Istanbul Technical University, 2007
M.S. in Biomedical Engineering, Boğaziçi University, 2011

Submitted to the Institute of Biomedical Engineering
in partial fulfillment of the requirements
for the degree of
Doctor
of
Philosophy

Boğaziçi University
2019

APPLICATION OF NEWBORN JAUNDICE DETERMINATION AND DESIGN OF A NONINVASIVE BILIRUBINOMETER

APPROVED BY:

Prof. Dr. Mehmed Özkan ....
(Thesis Advisor)

Prof. Dr. Ali Yekta Ülgen ....

Prof. Dr. Murat Gülsoy ....

Prof. Dr. Ahmet Ademoğlu ....

Assist. Prof. Dr. Murat Tümer ....

DATE OF APPROVAL: 13 June 2019

ACKNOWLEDGMENTS

I would like to thank all the people who contributed in some way to the work described in this thesis. First and foremost, I would like to express my sincere gratitude to my advisor Prof. Dr. Mehmed Özkan for the tremendous support during my Ph.D. study and related research, for his patience, motivation, and immense knowledge. His guidance helped me throughout the research and writing of this thesis.

Besides my advisor, I would like to thank the other members of my thesis committee: Prof. Dr. Ali Yekta Ülgen, Prof. Dr. Murat Gülsoy, Prof. Dr. Ahmet Ademoğlu and Assist. Prof. Dr. Murat Tümer for their insightful comments and encouragement, but also for the question which inspired me to widen my research from various perspectives.

I want to thank my loving and caring family. I am grateful to my parents for all their sacrifices and prayers. I am also grateful to them for teaching me to follow my dreams even when they go against the grain. Words cannot express my appreciation and love for my daughter Sena and son Mehmet. The motive of this dissertation was to be a role model for them.

Last, but by no means least, I am grateful to my wife Betül for her incredible support and encouragement. She was always there to give me the best advice. Thank you.

ACADEMIC ETHICS AND INTEGRITY STATEMENT

I, Yunus Karamavuş, hereby certify that I am aware of the Academic Ethics and Integrity Policy issued by the Council of Higher Education (YÖK) and I fully acknowledge all the consequences due to its violation by plagiarism or any other way.

Name : ______________________

Signature: ______________________

Date: ______________________

ABSTRACT

APPLICATION OF NEWBORN JAUNDICE DETERMINATION AND DESIGN OF A NONINVASIVE BILIRUBINOMETER

Newborn jaundice (hyperbilirubinemia), which is seen in 65% of healthy newborns, is usually a harmless condition and passes without any treatment. However, 5% of the jaundiced babies develop kernictures which may cause irreversible brain damage. Therefore, detection and follow-up of jaundiced babies are very important. The most common method for the evaluation and follow-up of neonatal jaundice is measuring the level of total serum bilirubin (TSB). Transcutaneous bilirubin (TcB) measurement, which is an alternative for jaundice detection and monitoring, is a safe, easy, painless, cost-effective and fast method as well as being noninvasive. The application of TcB measurement uses visible field reflection spectroscopy to determine the level of jaundice in newborns. The aim of this thesis is to design algorithms which can determine the level of jaundice by nonlinear approaches using diffuse reflection spectra obtained from a specially developed device. In order to achieve this, TcB and TSB measurements were taken from 314 infants and prediction algorithms were developed. The TcB values predicted by the designed algorithms were compared with the TSB values of the paired measurement. In addition, the performance of the designed algorithms was compared with the widely used JM-103 transcutaneous bilirubinometer. All designed algorithms can predict jaundice level with correlation values between 0.932 and 0.943. The results of the comparisons were found to be promising for the use of transcutaneous bilirubinometer devices.

Keywords: Newborn Jaundice, Transcutaneous Bilirubinometry, Nonlinear Regression Methods, Hyperbilirubinemia.

ÖZET

YENİDOĞAN SARILIĞI TESPİTİNİN UYGULAMASI VE NONİNVAZİF BİLİRUBİNOMETRE TASARIMI

Yenidoğan sarılığı (hiperbilirubinemi) sağlıklı yenidoğanların %65'inde görülmekte ve genellikle herhangi bir tedavi uygulanması gerekmeden kendiliğinden geçmektedir. Fakat bu yenidoğanların %5 kadarında kernikterus olarak bilinen kalıcı beyin hasarları ortaya çıkabilmektedir. Bu nedenle yenidoğan sarılığının tespit ve takip edilmesi büyük bir önem taşır. Yenidoğan sarılığını değerlendirmede ve takip etmede en yaygın olarak kullanılan yöntem, toplam serum bilirubin (TSB) düzeyini ölçmektir. Sarılık tespiti ve takibi için alternatif bir yöntem olan transkütan bilirubin (TcB) ölçümü ise non-invasif olmasının yanı sıra güvenli, kolay, acısız, düşük maliyetli ve hızlıdır. TcB ölçümü uygulaması yenidoğanlarda sarılık seviyesini belirlemek amacıyla görünür bölgede yansıma spektroskopisini kullanır. Bu tez çalışmasının amacı özel olarak geliştirilmiş bir cihazdan elde edilen difüz yansıma spektrumlarını kullanarak, lineer olmayan yaklaşımlar ile, sarılık seviyesini tespit edebilen algoritmaların geliştirilmesidir. Bu amaçla 314 bebekten TcB ve TSB ölçümleri alınmış ve kestirim algoritmaları geliştirilmiştir. Geliştirilen algoritmalar ile tahmin edilen TcB değerleri, ilgili ölçüme ait TSB değerleri ile kıyaslanmıştır. Ayrıca geliştirilen algoritmaların performansı, piyasada yaygın olarak kullanılmakta olan JM-103 transkutan bilirubinometre cihazı ile de karşılaştırılmıştır. Geliştirilen tüm algoritmalar 0.932 ile 0.943 arasında korelasyon değerleri ile sarılık seviyesini tahmin edebilmekte olup, bu karşılaştırma sonuçları transkütan bilirubinometre cihazlarının kullanımının artacağı yönünde teşvik edici görülmüştür.

Anahtar Sözcükler: Yenidoğan Sarılığı, Traskütan Bilirubin Ölçümü, Non-lineer Yaklaşım Metodları, Hiperbilirubinemi.

TABLE OF CONTENTS

LIST OF FIGURES

LIST OF TABLES

LIST OF SYMBOLS

r	Correlation coefficient
μ_a	Absorption coefficient
μ_s	Scattering coefficient
μ_s'	Reduced scattering coefficient
l_s'	Mean free path
f_{me}	Volume fraction of epidermal melanin
f_{bl}	Volume fraction of blood
c_{bili}	Bilirubin concentration
λ	Wavelength
g	Anisotropy factor
I_0	Initial light intensity
I	Light intensity
C_{Mie}	Mie constant
$C_{Rayleigh}$	Rayleigh constant
n	Refractive indices
$D(s)$	Actual surface spectra
$M(s)$	Measured surface spectra
$H(s)$	Reference measurement spectra
$N(s)$	Dark measurement spectra
$K(*)$	Kernel function
ϵ	Error tolerance
p	Level of marginal significance
$\overline{x}$	Mean of x values
$\overline{y}$	Mean of y values
ξ_i^*	Slack variable, upper training error
ξ_i	Slack variable, lower training error

LIST OF ABBREVIATIONS

AAP	The American Academy of Pediatrics
ADC	Analog Digital Converter
ANN	Artificial Neural Network
CAGR	Compound Annual Growth Rate
CIs	Confidence Intervals
CMOS	Metal–Oxide Semiconductor
DRS	Diffuse Reflectance Spectroscopy
FDA	Food and Drug Administration
GUI	Graphical User Interface
HPLC	High-Performance Liquid Chromatography
LCD	Liquid Crystal Display
LED	Light Emitting Diode
MAE	Mean Absolute Error
MPR	Multiple Polynomial Regression
NA	Numerical Aperture
NIH	National Institutes of Health
PCA	Principal Component Analysis
PLS	Partial Least Squares
RBF	Radial Basis Function
RTE	Radiative Transfer Equation
SD	Standard Deviation
SNR	Signal to Noise Ratio
SVR	Support Vector Regression
TcB	Transcutaneous Bilirubin
TSB	Total Serum Bilirubin
USB	Universal Serial Bus
VIS	Visible Spectrum

1. INTRODUCTION

1.1 Overview of Newborn Jaundice Determination and Noninvasive Bilirubinometers

Bilirubin is a yellow substance which is created in the blood when the hemoglobin breaks down. In newborns, bilirubin formation is 2-3 times faster than in adults due to the shorter life span of fetal hemoglobin compared to adult hemoglobin [1]. The fact that the immature liver of a newborn often cannot remove excess bilirubin quickly enough leads to bilirubin accumulation in the body of the baby. This overabundance of bilirubin is the origin of neonatal hyperbilirubinemia (jaundice). This is a common and generally harmless clinical condition that occurs in more than 65-70% of healthy term newborns while 5-10% of the cases may result in kernicterus, which can cause irreversible brain damage [2]. Therefore, detection and accurate quantification of the bilirubin concentration is vital to prevention of hyperbilirubinemia by providing adequate treatment such as phototherapy and exchange transfusion. The American Academy of Pediatrics (AAP) recommends that all infants should be examined for jaundice within the first few days of birth [3].

Clinical evaluation of jaundice generally involves visual estimation of the yellowness of the newborn skin by experienced physicians or nursing staff. Nevertheless, quantification of jaundice based on visual assessment of the bilirubin level is biased, inaccurate, and confounded by skin colour and hemoglobin. Currently, total serum bilirubin (TSB) is the gold standard, which is applied by capillary heel-stick blood sampling method. However, being an invasive method, blood sampling for the determination of TSB may lead to risk of infection, discomfort or pain in infants [4]. Moreover, measurement of TSB through blood sampling is not only stressful for parents but also laborious and incapable of giving immediate results. To overcome these drawbacks, transcutaneous bilirubin (TcB) measurement, also called transcutaneous bilirubinometry, is being used to determine the bilirubin level. This is a noninvasive and painless method with instant measurement results. The use of transcutaneous bilirubinometers is recommended in clinical practice guidelines on the management of jaundice [3]. Examples of transcutaneous bilirubinometers currently available in the market and approved by U.S. Food and Drug Administration are BiliChek (BC; Respironics, Marietta, GA, USA) and the Draeger JM-103 (Draeger Medical Inc, Telford, Pennsylvania) [5]. A research study found that TcB measurements correlate well with TSB levels, with correlation coefficients between 0.77 and 0.97 [6].

TcB measurement is based on reflectance spectroscopy, which is a non-destructive and noninvasive method for obtaining diagnostic information based on the biochemical composition of and the physiological information from the tissue. In this method, a light source is used to illuminate the biological tissue. As the incident light penetrates the tissue, the direction of propagation changes randomly due to refractive index variations in the layers beneath. After several scattering events, some of the light re-emerges from the surface. The intensity of this reflected light carries information regarding the absorption and scattering of light by the subcutaneous tissue that can be correlated with the morphology to determine the concentration of chemicals such as bilirubin in the tissue. There are several methods that use reflectance spectroscopy for determination of bilirubin level, such as diffusion theory and Monte Carlo simulation look-up table. Diffusion theory models the propagation of light in the tissue and an inverse model is used to determine the jaundice level from the measured reflectance spectrum [7]. In Monte Carlo simulation approach, neonatal skin is modelled as a three-layer structure and diffuse reflectance is simulated in the spectral region 400-700 nm with known neonatal skin optical properties. Then, a look-up table is created by varying the bilirubin concentration [8].

1.2 Motivation and Objectives

The use of transcutaneous bilirubinometry cannot replace TSB yet as stated in [9], and hence it has limited clinical value. It is stated elsewhere that combining an information-rich analytical technique, such as reflectance spectroscopy, with efficient statistical tools can enable the development of an efficient method to determine the concentration level of a substance accurately [10, 11]. The amount of bilirubin, which causes newborn jaundice when in an overaccumulation state in the blood, can be measured by reflectance spectroscopy in a similar way. In TcB measurements, the jaundice level is determined by measuring the concentration of bilirubin in the extravascular region. As the bilirubin concentration in this area is not linearly dependent on the bilirubin concentration in the blood, the relationship between TcB and TSB levels is nonlinear [9]. Therefore, in this study nonlinear regression methods are proposed to determine the newborn jaundice level with improved accuracy in order to increase the clinical value of noninvasive bilirubinometers.

In determining the level of jaundice, the reflected spectra from the newborns' skin are used. For this purpose a prototype device had to be built to collect the data for use in the designed nonlinear bilirubin detection algorithms. This prototype device was developed to make use of reflectance spectroscopy, and a typical measurement setup in this device comprises three main components: a light source to illuminate the skin, a light transmission probe to deliver the incident light and to collect the reflected light, and a spectrometer to evaluate the reflected light.

By using this prototype device, we carried out a large-scale clinical study to measure reflectance spectra of jaundiced newborns to design bilirubin detection algorithms. The designed fitting algorithms are compared by evaluating their predictive performance in determining the jaundice level in newborns. We also compare the predicted results with the measured results of Draeger JM-103 which is a commonly used commercially available transcutaneous bilirubin measurement device. The comparison was done by calculating the correlation coefficients (r), mean absolute error (MAE), and bias.

1.3 Outline of the Dissertation

In this first section, I present an overview of newborn jaundice determination and noninvasive bilirubinometers. This chapter also contains the motivation and objectives of the study.

Chapter 2 summarizes the current state of the art in newborn jaundice, skin tissue optics, and diffuse reflectance spectroscopy. The types of newborn jaundice and current methods in jaundice determination are investigated in detail. Then, skin tissue optics together with a description of the skin physiology, light interaction with tissue and neonatal skin properties are investigated. Also, the literature on bilirubin, hemoglobin and melanin reflectance spectra is reviewed. Then, diffuse reflectance spectroscopy is described. A typical diffuse reflectance measurement setup is given and Monte Carlo simulations are reviewed.

Chapter 3 describes our studies on designing a diffuse reflectance measurement system. Also, this chapter contains a published work titled "Design of a New Optic Probe for Diffuse Reflectance Spectroscopy". In this paper, design of a new optical probe for applying diffuse reflection spectroscopy is presented.

Chapter 4 presents the jaundice determination algorithms designed in this dissertation. The design of these algorithms was published as a journal article, "Newborn Jaundice Determination by Reflectance Spectroscopy Using Multiple Polynomial Regression, Neural Network, and Support Vector Regression". In addition, the predictive performance of the designed algorithms were analysed. The obtained results were encouraging towards increasing the clinical usage of transcutaneous bilirubinometers since all the designed methods accurately predict the jaundice level.

Chapter 5 provides a general summary and conclusion of the dissertation as well as suggestions for future development and directions for the newborn jaundice determination and noninvasive bilirubinometry.

2. BACKGROUND

2.1 Newborn Jaundice

Newborn jaundice, or hyperbilirubinemia, is a clinical problem, which is encountered frequently during the neonatal period, especially in the first week after birth, however, it is a benign problem most of the time [3, 12]. Approximately 5% to 10% of them develop significant clinical hyperbilirubinemia, which necessitates phototherapy or exchange transfusion. In this condition, TSB rises above the 95^{th} percentile for age (high-risk-zone) [13, 14]. Large amount of bilirubin in the blood is the root cause of neonatal jaundice. When this overaccumulated unconjugated bilirubin gets out of the vein, it deposits near the skin surface and mucous membranes, and leads to discoloration of skin and yellowing of sclera as seen in Figure 2.1 [15]. For this reason, it may be a concern for physicians and cause anxiety to parents.

Bilirubin is not only a distressing molecule that leads to critical results but also, like uric acid, an important antioxidant that circulates in the biological system of the newborn [17]. Accordingly, high levels of bilirubin may be toxic, and therefore, inhibit the development of the central nervous system and may result in behavioral and neurological deterioration, known as kernicterus, even in newborns [2, 18].

2.1.1 Types of Hyperbilirubinemia

Some of the reported jaundice types are physiological jaundice, breast feeding and human milk jaundice, and pathological jaundice.

Physiological jaundice is the most frequent type of newborn hyperbilirubinemia, but without any serious consequences [19]. Physiological jaundice occurs in infants for various reasons. One of the reasons is that the rate of bilirubin production in

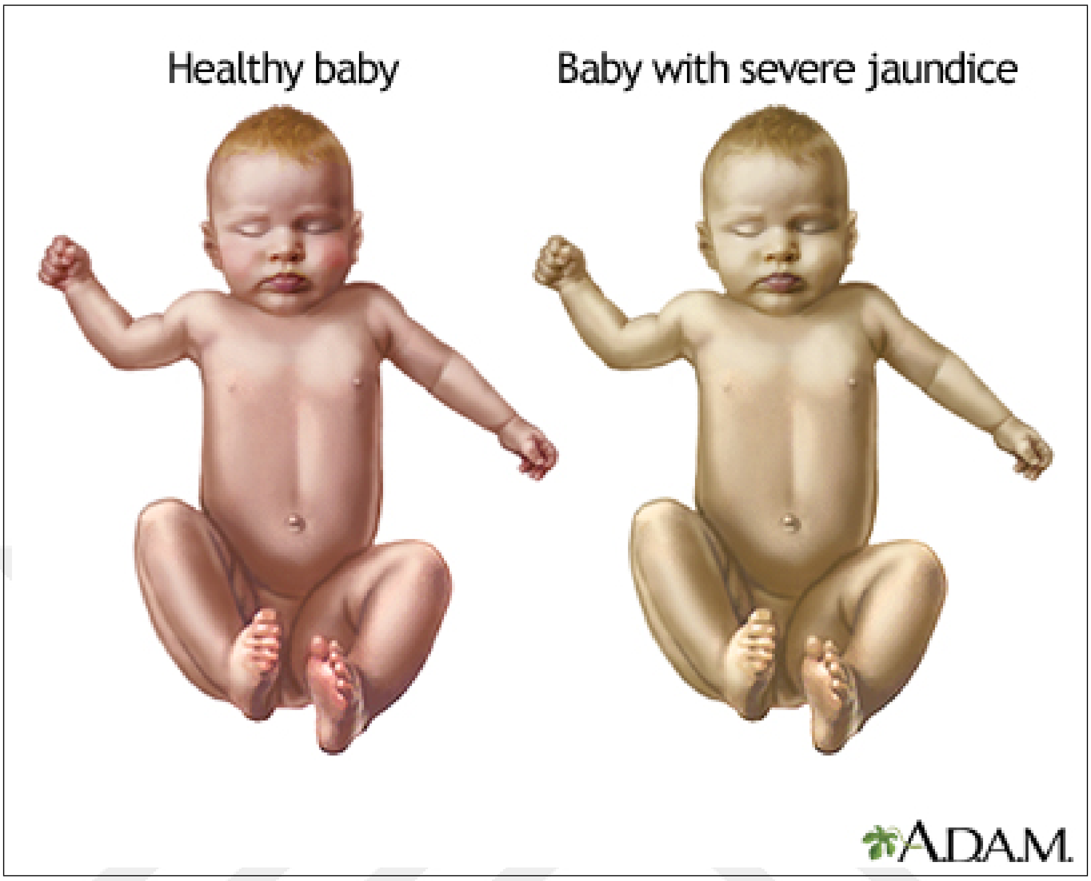

Figure 2.1 Healthy and severely jaundiced baby [16].

infants is high, but they do not have the ability to rapidly eliminate bilirubin from the body. This is caused by the relatively low activity of the glucuronosyl transferase enzyme which normally converts unconjugated bilirubin to conjugated bilirubin that can be discharged into the gastrointestinal tract [20]. After a few days of the birth, this enzyme gains normal functionality. Another cause of physiological jaundice is the shorter life span of the red blood cells. While the life span of red blood cells in adults is 100 to 120 days, it is 80 to 90 days in infants [21].

Breast feeding or breast milk jaundice is another type of newborn jaundice that may be observed in the first postnatal week and may be due to caloric deficiency and/or insufficient frequency of feeding. Successful breastfeeding helps in preventing or treating this type of jaundice. Within the first few days of birth, feeding frequency of infants should be at least 8 to 12 times to help boost breastfeeding [22]. Human milk (breast milk) jaundice occurs later in newborn period from the sixth through the fourteenth day after birth and may persist for 1 to 3 months. The underlying cause of breast milk jaundice is not entirely clear. It is believed that substances in human milk, such as beta-glucuronidases and nonesterified fatty acids, may inhibit normal bilirubin metabolism [23, 24, 25]. This phenomenon might be the main reason for this type of jaundice.

All types of jaundice are considered to be pathological, except physiological and breast feeding or breast milk jaundice. In pathological jaundice, the bilirubin levels are not in the normal range and intervention is required [9]. The level of TSB rises rapidly (more than 5 mg/dl per day) within 24 hours after birth. The most likely reason is blood incompatibility or liver disease. Emergency medical attention is required, and exchange transfusion may have to be performed.

2.1.2 Jaundice Determination

The most likely approach to diagnose newborn jaundice is visual examination. Visual examination has a high negative predictive value, which means that infants who do not seem visually jaundiced are very unlikely to have clinically significant jaundice. But, it is not possible to determine the severity of hyperbilirubinaemia by visual examination. For this reason, visual examination alone is not sufficient for detecting jaundice requiring phototherapy and and may even increase the risk for babies to develop kernicterus [26].

Apart from visual examination, measurement of TSB level by a blood test or by using a transcutaneous bilirubinometer can better diagnose hyperbilirubinaemia that requires treatment or further monitoring. These kinds of measurements give quantitative results indicating the severity of jaundice.

High-pressure liquid chromatography bilirubin (HPLC-B) measurement in the laboratory is considered the gold standard method for TSB estimation. This method is not affected by interference from hemoglobin or lipemia; however, it is very costly and labor-intensive, therefore, can not be used routinely [27]. On the other hand, direct spectrophotometry for the measurement of TSB is simple and rapid in that it can be assessed with a minimal sample for analysis [28]. In this method, multiple wavelength readings on 454 nm and 528 nm, at which bilirubin and hemoglobin absorption are dominant, are made. In addition, algorithms to correct the hemoglobin effect on the obtained absorption spectra are used. Unfortunately, other molecules, such as carotenoids, also have dominant absorption at 454 nm wavelength so that this method can be used only with infants of less than 2–3 weeks of age [27].

2.1.3 Transcutaneous Bilirubinometry

Transcutaneous bilirubinometry is a noninvasive, fast, and relatively inexpensive method that can be used in determining bilirubin level [29, 30]. This method is applied by an easy-to-use handheld device, which is placed on the newborn's skin (optimally on the forehead or sternum). While each transcutaneous bilirubinometer has a different working principle, the main approach is the same. These devices illuminate the skin surface of the neonates and measure the specific wavelength that is reflected. Then the obtained spectra are analyzed and serum bilirubin level is determined. Draeger JM-103 and JM-105, Mennen Bilicare, Philips BiliChek, and Medick BiliMed are examples of transcutaneous bilirubinometer that are currently in the market [31, 32].

Bilichek scans the entire visible light spectrum while illuminating the skin and determines the bilirubin level by subtracting the light reflected by confounding molecules such as hemoglobin or melanin from the total reflected spectrum. Once the obtained wavelengths have been quantified, a microprocessor analyzes the data and predicts the TcB measurement results. It should be calibrated with a calibration tip before each usage.

Bilimed contains ten light emitting diodes (LED) to illuminate the newborn skin. Reflected light is gathered by a silicon diode and converted into digital form to find the bilirubin level.

Of JM-103 and JM-105 manufactured by Draeger, JM-105 is the newer device and uses a xenon lamp for the illumination of skin. Reflected light is gathered by two photo diodes that work at 460 nm and 540 nm wavelength. There are two optical paths, one shorter than the other, for the collection of reflected light. By measuring the difference between the spectra obtained from the two pathways, the effect of melanin and hemoglobin is eliminated and the amount of bilirubin built up mainly in the deeper subcutaneous tissues is deduced. After converting the reflected light detected by two photodetectors into digital signals, the bilirubin level is determined.

Recently, there are some research studies that use smart phones as screening tools for neonatal hyperbilirubinemia by processing the images produced by the cell phone camera [33, 34, 35]. A color calibration card which is the size of a business card is put on the newborn's skin while taking the photo. The results show that a smart phone which has a consistent light source may be used as a simple tool for monitoring jaundice. Also, it is being planned to do the analysis in the cloud so that algorithms can be amended over time. However, this method needs some improvements before being used in clinical applications.

2.2 Skin Tissue Optics

In this section, main properties of the skin physiology and interaction of light with skin tissue are described. These are important for understanding and interpreting the experimental data and constructing theoretical models. Also, they are essential for being able to use spectroscopy for diagnostic applications.

2.2.1 Skin Physiology

Human skin is the outer layer of human body that protects the human organism including muscles and organs against environmental factors such as infections, excessive optical radiation, water loss or heat. The skin has a three layer structure:

epidermis, dermis, and subcutis. Epidermis is the outermost skin layer and typically has thickness of 50 – 80 μm. It consists of five sub-layers, which are, from the surface, stratum corneum, stratum lucidum, stratum granulosum, stratum spinosum, and stratum basale. One type of cell in the stratum basale are the keratinocytes. These cells reproduce through mitosis and produce keratin. They are responsible for keeping the skin and the tissues under it waterproof. Two other cell types found in basal layer are Merkel cell and melanocyte cell. Merkel cells act as receptors and their function is to stimulate the sensory nerves that produce the perception of the sense of touch. Melanocytes, on the other hand, produce the pigment melanin that is responsible for giving the hair and skin their color [36]. Therefore, in this thesis particular attention was paid to pigment melanin and its absorption spectra.

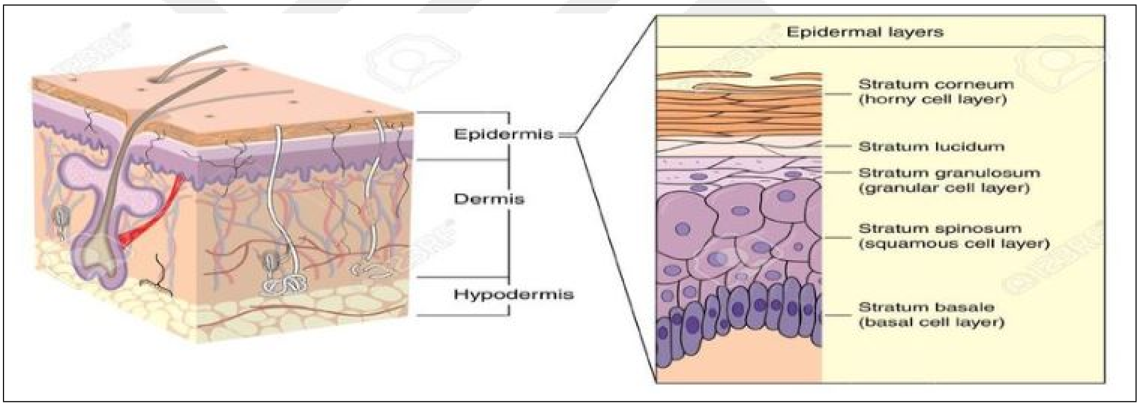

Figure 2.2 Cross section of human skin [37].

The pigment melanin is released in vesicles called melanosomes. The amount, shape and size of the melanosomes have a strong effect on the human skin color, which is genetically determined. Caucasian melanosomes contain larger amount of melanin granules, but less total melanin than negroid or mongolian melanosomes [38]. While caucasian melanosomes have a long axis with a length of 400 nm and can be seen as clusters, negroid melanosomes are larger having a long axis with a length of 800 nm and not in clusters. The concentration of melanosomes in the skin varies with body site, with the highest concentration level in areas exposed to sun. However, race has no effect on the concentration of melanosomes [39]. The absorption spectra of melanin is described in the following sections.

Dermis layer, generally 1 mm to 4 mm, is thicker than the epidermis and has a more complex structure. It has less number of cells and is mainly made up of hair follicles, lymphatics, sweat glands, elastic and collagen fibers, sensory nerve systems, blood vessels, and connective tissue [40]. The thickness of this layer varies with age, body site, gender, and smoking habits [41].

The deepest layer, subcutaneous tissue, also known as the hypodermis, is the innermost layer of skin. It mainly consists of fat and connective tissues that contain larger blood vessels and nerves, and it provides insulation to help regulate body temperature and acts as a shock absorber. The thickness of this layer can be up to 8 mm [42].

The concentration and the depth of the chromophores, mainly melanin, hemoglobin, and bilirubin, in these three skin layers have a remarkable effect on skin reflectance in VIS. Both absorption and scattering properties of these chromophores and skin structure affect skin reflectance spectra. The experimentally obtained absorption spectra, which can be expressed as molar extinction coefficient values, are available in literature [43].

2.2.2 Interaction of Light With Tissues

Light is electromagnetic radiation in the wavelength range of approximately 400–760 nm. Visible light (VIS) is the spectrum that we can see and has a role in producing the sense of sight. The main source of VIS is the sun. There are also other sources of VIS, both natural and man-made [44].

Visible light interacts with the skin through reflection, absorption, scattering, and transmission. The interaction is determined by the wavelength of the light and the optical properties of the skin. Absorption and scattering are the most prevalent

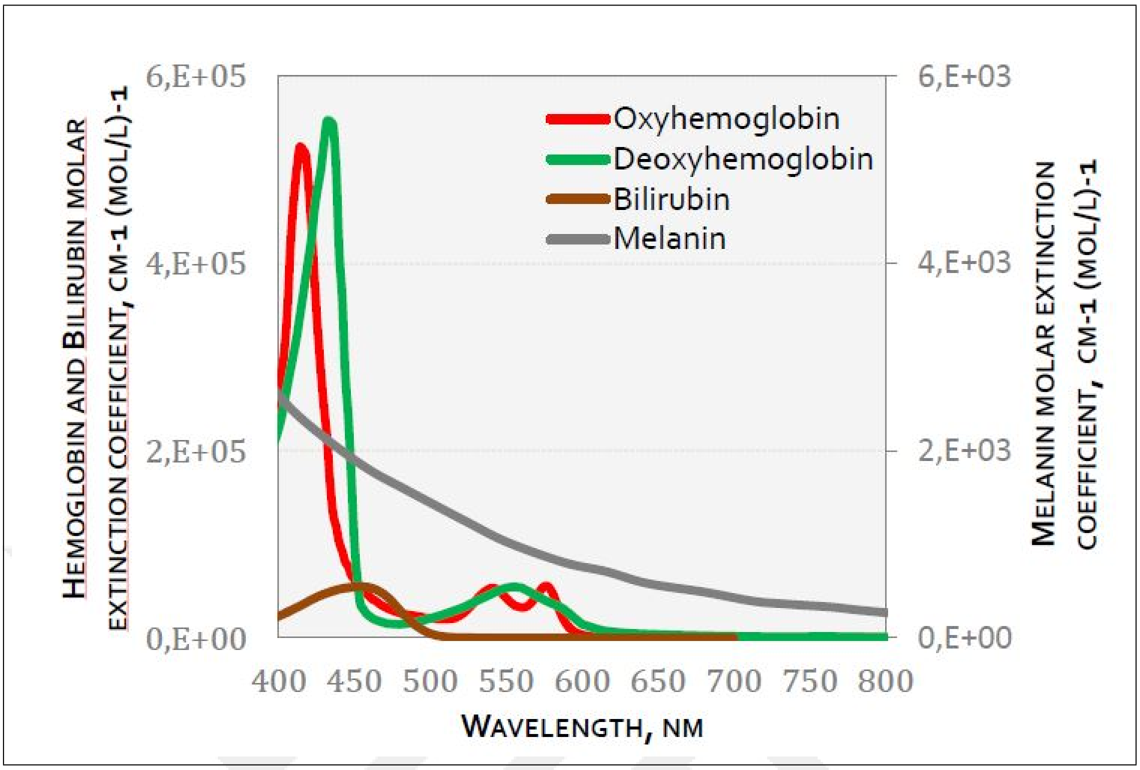

Figure 2.3 Molar extinction coefficients of oxy and deoxyhemoglobin, bilirubin, and melanin in the visible spectral range [43].

interactions when an incident light ray hits the biological tissue. The composition of the biological tissue determines the shape of absorption and reflectance spectra. The spectral feature of a chromophore can be modelled mathematically with absorption and scattering coefficients.

Scattering occurs due to a difference between the refractive indexes of two neighbouring media. It strongly depends on the size of the scatterer. Mie scattering is the dominant scattering event in human tissue when the scattering particle's size is similar to or larger than the wavelength. Mie scattering is generally forward directed. Rayleigh scattering is another scattering event that occurs in human tissue with particles that have a radius less than approximately 1/10 the wavelength of the incident light. The sizes of hemoglobin, bilirubin and melanin molecules are about a couple of nanometers, and therefore, they are considered to be Rayleigh scatterers [45].

When a scattering event occurs, the incident light changes its direction with an angle θ. The distance that is traversed by this scattered light in each scattering event is called the mean free path $l_s = 1/\mu_s$ where μ_s is the scattering coefficient. The angular distribution of the scattering angles, anisotropy factor g, can be introduced as in Eq. 2.1, as the average cosine of the scattering angles [46].

$$g = \overline{cos(\theta)} \tag{2.1}$$

Value of the anisotropy factor in the visible spectral range perceived by human beings is approximately 0.8. It is wavelength dependent and can be experimentally formulated [47] and can be expressed as in Eq. 2.2

$$g = 0.62 + 29 * 10^{-5}\lambda \tag{2.2}$$

where λ is the wavelength in nm. Incident photons lose their direction with a certain depth, which is called reduced scattering mean free path and is defined by Eq. 2.3

$$l'_s = l_s/(1-g) \tag{2.3}$$

The reduced scattering coefficient is given by

$$\mu'_s = 1/l'_s \tag{2.4}$$

Absorption coefficient is a representative term for measuring the rate of decrease in the intensity of light as it penetrates through a given substance before being absorbed. The absorption in a homogeneous, non-scattering medium can be simply defined by the Lambert-Beer law, which states that the initial light intensity I_0 decreases exponentially after traveling a distance x through a medium with an absorption coefficient, μ_a.

$$I(x) = I_0 e^{-\mu_a x} \tag{2.5}$$

Skin contains various chromophores such as hemoglobin, melanin, and bilirubin that cause absorption and scattering events of incident light. The optical properties of these molecules are important in reflectance spectroscopy; therefore, they will be presented in the following sections.

2.2.2.1 Melanin. Melain is mostly responsible for the darkness of skin and it is the main absorber in the epidermis layer [36]. In 1975, Fitzpatrick defined the skin types based on varying amounts of the pigment melanin on a skin type scale of I-VI [48]. On this scale, type I refers to extremely sensitive skin that always burns and never tans while the opposite end of the scale, namely type VI, refers to very resistant skin that never burns and is deeply pigmented.

Melanin has a broad absorption band ranging from the ultraviolet to the near infrared [49]. Melanin absorption is inversely proportional to wavelength and the relation is given as $\lambda^{-3.56}$ [50]. Therefore, the absorption value at a single wavelength is sufficient to define the absorption of melanin throughout the whole spectrum. Generally, its absorption is measured at 694 nm. The general formula of the melanin absorption is given by Eq. 2.6

$$\mu_{a,m} = 225m^{-1}(\frac{694nm}{\lambda})^{3.46} \tag{2.6}$$

According to this formula, the melanin absorption coefficient is $\mu_{a,m} = 225m^{-1}$ at 694 nm for fair Caucasian skin. Newborn skin has less melanin concentration than adult skin [51].

2.2.2.2 Hemoglobin. Hemoglobin is the dominant absorber molecule in blood. Its function is to transport oxygen from the lungs to the tissues throughout the whole human body and return carbon dioxide back to the lungs. Hemoglobin without bound oxygen is called deoxyhemoglobin (Hb) and shows a dark red, bluish livid color while hemoglobin with bound oxygen is called oxyhemoglobin (HbO_2) and has a bright red color [52, 53]. The absorption spectra of oxyhemoglobin and deoxyhemoglobin in VIS are different. As seen in Figure 2.3, deoxyhemoglobin has absorption peaks at 550 nm and 760 nm while oxyhemoglobin has absorption peaks at 548 nm and 576 nm. Both chromophores have high absorbing ability in the 400-450 nm spectral range with absorption peaks at 410 nm for oxyhemoglobin and 430 nm for deoxyhemoglobin [43].

There are other forms of hemoglobin such as methemoglobin, sulfhemoglobin in a negligible amount in blood (less than 1% of total hemoglobin) [54]. As such, they are not taken into account in reflectance measurements. The absorption coefficient of hemoglobin is strongly dependent on oxygenation, which varies with skin depth.

2.2.2.3 Bilirubin. Bilirubin is produced when hemoglobin breaks down [55]. Normally, bilirubin is transported to the liver where it is further processed to become water-soluble and it is discharged in the bile. However, this process does not work properly in newborns. In the uterus, the baby has a large amount of hemoglobin to increase transportation of oxygen from the placenta to the baby. After birth, when babies start to breathe and use their own lungs, this excessive amount of hemoglobin is no longer needed and is broken down. If it is not discharged as fast as it is produced, bilirubin accumulates in the blood and causes newborn jaundice. The treatment of jaundice might be through light therapy, intravenous immunoglobulin or, in severe cases, blood transfusion [56].

Bilirubin is created in the human body not only during jaundice condition but also when bruise color changes into yellow. In 1847, Virchow found that bilirubin is the reason of yellow color in old bruises [57]. When skin is bruised, hemoglobin is broken down by macrophages in the injured skin tissue. A systematic process of hemoglobin breakdown in bruised skin is shown in Figure 2.4.

Bilirubin has a characteristic absorption peak at 460 nm in the absorbance spectrum. Hence, accumulation of bilirubin near the skin surface can be observed by reflectance spectroscopy in the wavelength range 450-480 nm. Hemoglobin and melanin also have absorption in this range. Therefore, one should take into account the effects of these molecules on the obtained reflectance spectra while determining the bilirubin

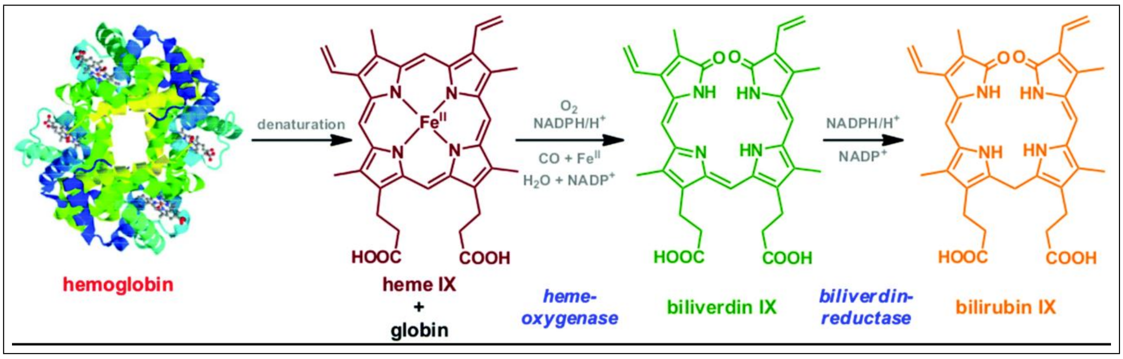

Figure 2.4 Overview of chemical breakdown of hemoglobin [58].

absorption spectrum.

2.2.3 Neonatal Skin Properties

In literature there are many research papers about skin optics but very few about neonatal skin optical properties, such as μ_a and μ_s. In a research study, Saidi used an integrating sphere setup to measure the absorption coefficient and reduced scattering coefficient as a function of gestational maturity [59]. In his study, he used the visible spectrum and concluded that the absorption coefficient is independent of gestational maturity while reduced scattering coefficient, $\mu_s(1-g)$, increases directly with the gestational maturity of infants. The scattering coefficient with respect to gestational maturity is formulated as follows:

$$\mu_s(1-g) = y(\lambda) + m(\lambda)maturity \tag{2.7}$$

where $\mu_s(1-g)$ is in cm^{-1} and *maturity* is in weeks. The empirical fit of y(λ) as a function of wavelength is described by Eq 2.8,

$$y(\lambda) = 22.5 - 0.14267928\lambda + 0.000129357\lambda^2 \tag{2.8}$$

The definition of slope, m, is given by Eq. 2.9

$$m(\lambda) = 2.978 - 0.0029985\lambda \tag{2.9}$$

where wavelength, λ, is expressed in nm [59].

Later, Saidi and his colleagues carried out another study with 22 skin samples and described scattering of light in biological tissue in terms of Mie and Rayleigh scattering [60]. In their study, the reduced scattering coefficient, μ_s', is calculated as

$$\mu_s' = C_{Mie}(1 - 1.745 * 10^{-3} * \lambda + 9.8443 * 10^{-7} * \lambda^2) + C_{Rayleigh} * \lambda^{-4} \tag{2.10}$$

where C_{Mie} is the Mie constant and $C_{Rayleigh}$ is the Rayleigh constant. The constants take the values $C_{Mie} = 6800\ m^{-1}$ and $C_{Rayleigh} = 9.5x10^{13}\ nm^4/m$ for a gestational age of 39 weeks [60]. Saidi et al. derived these formulas through laboratory experiments that were performed *in vitro* on excited non-pigmented skin. However, optical properties may be different for *in vivo* measurements.

2.3 Diffuse Reflectance Spectroscopy

Reflection is the scattering of light back in the direction of the incident light. This optical phenomenon can occur in two ways: specularly and diffusely as shown in Figure 2.5. Specular reflection occurs when the incident light hits a smooth, polished surface such as a mirror or a calm body of water. Light reflection from mat, rough surfaces such as clothing, paper, and asphalt roadways leads to a type of reflection known as diffuse reflection [61]. A reflectance spectrum is obtained by the collection and analysis of electromagnetic radiation reflected from the surface as a function of wavelength usually in nm.

Diffuse reflectance spectroscopy (DRS), also known as elastic scattering spectroscopy, is a non-contact, noninvasive, and low-cost spectroscopic technique that provides optical characterization of the tissue under test. DRS has been used extensively for the noninvasive study, analysis, and characterization of biological tissues. This technique gives information about absorption and scattering properties of light by the tissues. Biomedical applications of spectroscopy include studies on colon, esophagus,

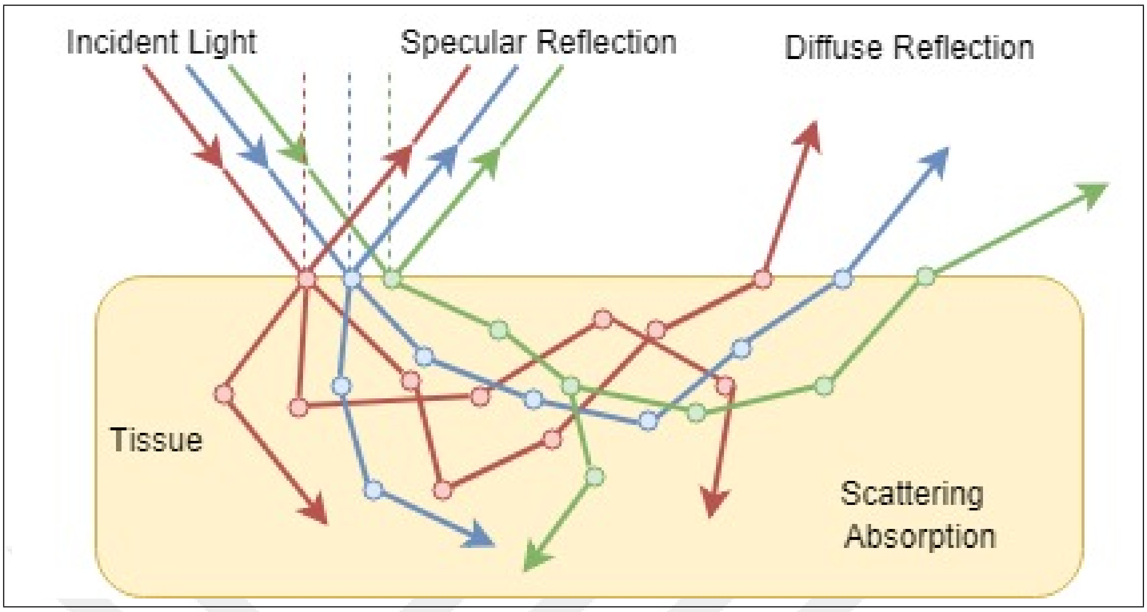

Figure 2.5 Specular and diffuse reflectance. While some of the photons are reflected from the surface of the tissue (specular reflection), some of them come from the deeper tissue and exit from the skin surface (diffuse reflection).

stomach, bladder, cervix, ovaries, breast, brain, liver, pancreas, heart, oral tissues, and skin [62, 63, 64, 65, 66]. DRS has some advantages over other spectroscopic techniques, such as being simple, scalable, and having compact instrumentation while demonstrating high accuracy characterization of both the optical absorption and the scattering properties of tissue [67]. Transcutaneous bilirubinometry is an example where DRS has a diagnostic application.

A typical measurement setup for reflectance spectroscopy consists of a light source for illuminating the skin, a detector for evaluating the reflected light, and an optic probe for delivering and collecting the reflected light. The light source can be a halogen lamp, a tungsten lamp, a light emitting diode (LED), etc. The detector can be a photodetector or a spectrometer. Generally, fiber-optic cables are used as optic probes for light transmission [68, 65, 69]. Optic probes consist of two separate light paths: one for delivering the light to the target biological tissue and one for collecting the light coming from the target biological tissue.

Collected light from the tissue being examined carries information about the absorption and scattering of light in the medium under study. This information can be correlated with morphology and biochemical composition so that the state of the biological tissue can be understood. If the scattering properties of a tissue are known, the absorbance within that tissue can be deduced from a single reflectance value. Many algorithms have been developed for the interpretation of reflected spectra. Using model-based techniques, statistical approaches, or nonlinear mathematical methods such as multivariate analysis, optical properties of the sample can be extracted from the distribution of light in the tissue. This yields valuable diagnostics information, such as the health state of the tissue or the concentrating of the chromophores deep within the tissue. Blood, melanin and bilirubin are examples of chromophores whose concentration can be determined using DRS in VIS.

Generally, DRS systems are categorized by the type of light source they use. Pulse lasers, intensity modulated lasers and continuous wave are examples of light sources used in DRS. DRS measurement systems that employ pulse lasers and intensity modulated lasers are categorized as time-domain and frequency-domain, respectively [70, 71]. DRS systems employing continuous wave light sources are categorized as steady-state technique [72]. Depending on the light source used, DRS has its own advantages and disadvantages. For example, time-domain DRS systems that use pulse lasers and time correlated single photon counting modules can detect photons that travel through the tissue in picosecond level. Despite the fact that this technique has high sensitivity to the absorption and scattering variation in tissues, its relatively high system setup cost prevents its wide spread use. Contrarily, spatially resolved DRS systems that use continuous light sources have low system cost. However, since the system setup requires several source-detector separations typically in the range of 1 to 20 mm, a more complicated multiple-fiber configuration is needed [73, 74].

2.3.1 Diffuse reflectance measurement setup

A typical DRS measurement setup is seen in Figure 2.6. As depicted in this figure, the tissue under interest is illuminated by a light source through the outer optic fibers colored yellow. The inner optic fiber colored blue gathers the reflected light that comes from deep within the tissue and transfers it to the detector. Here, the obtained spectra are converted into electronic signals to be further processed in the processing unit.

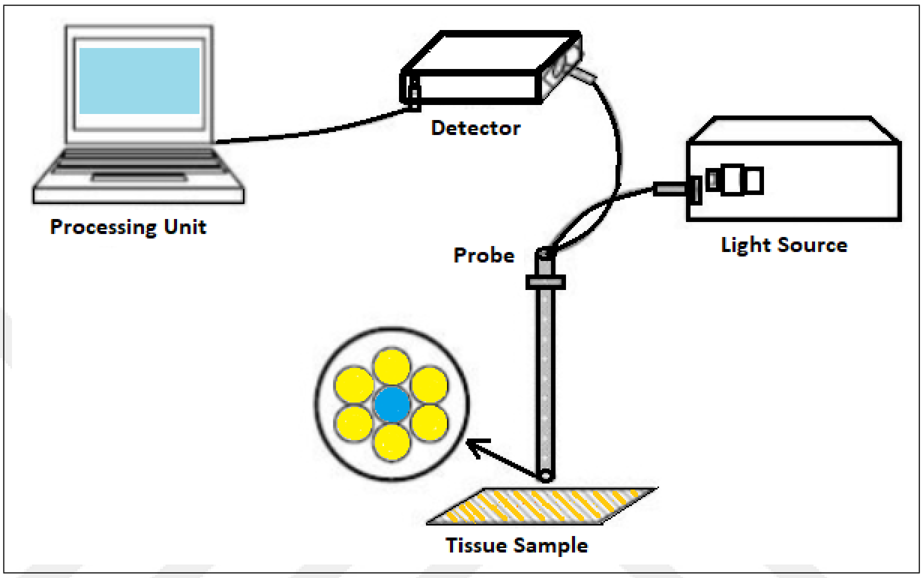

Figure 2.6 Experimental setup for diffuse reflectance measurements, which includes a light source, a compact detector, a fiber-optic probe, and a computer for data acquisition.

In the processing unit, raw reflectance spectra are corrected for system dark current and normalized to the spectrum obtained from the light source reflected on a white reference standard material. As a result, the actual spectrum of the target surface is obtained.

2.3.2 Monte Carlo Simulations

Monte Carlo simulations were first proposed by Metropolis and Ulam to simulate physical processes that cannot easily be predicted due to the intervention of random variables [75]. It is possible to model photon propagation with Monte Carlo Methods to simulate photon transport. In other words, it is possible to simulate the "random walks" that photons make as they travel through a turbid medium containing absorption and scattering events. Statistical calculation of probabilities of scattering and absorption events determines the path of each photon. Movement of a photon is based on a set of rules that are defined by probability distributions, which describe the step size of photon movement through the sites of photon-tissue interaction and angular deflection when a scattering event occurs. This is very similar to modeling photon transport analytically by the radiative transfer equation (RTE), which describes the movement of photons through the tissue using differential equations [76]. However, mathematical formulation of the RTE is generally not possible for some geometries. Diffusion approximation technique can be used to simplify the RTE, but this method introduces many inaccuracies, especially near sources and boundaries. In contrast, Monte Carlo simulations can be made relatively accurate by increasing the number of photons used [77].

In the application of Monte Carlo simulations, numerous photons are inserted into the tissue at a location determined by x, y, z coordinates, in other words, projection of the trajectory onto x, y and z axes. Once inserted, the photon travels a distance (Δs) where events such as scattering, absorption, propagation, internal reflection, or transmission out of the tissue may occur. The inserted photon moves continuously until it either is absorbed by the tissue or escapes from the tissue. Reflection or transmission event of the photon is recorded if the photon escapes from the tissue. If it is absorbed, the position of the absorption is recorded. This process is repeated until a certain number of photons have been propagated. The number of photons required for a simulation depends largely on the desired precision and the spatial or temporal resolution. As the number of photons increases, the obtained reflection, transmission and absorption profiles will approach their true values. Figure 2.7 depicts the flow chart of a Monte Carlo program. More detailed information about the parameter initialization and processes in the flowchart can be found in [78].

The application of Monte Carlo simulation on newborn skin is a special case and it was studied previously by Wang et al. [8]. Monte Carlo simulations would be very helpful in acquiring a better understanding of the melanin, hemoglobin and bilirubin reflectance spectra. In the following sections we will present these simulations with varying concentrations of these chromophores and discuss the obtained reflectance

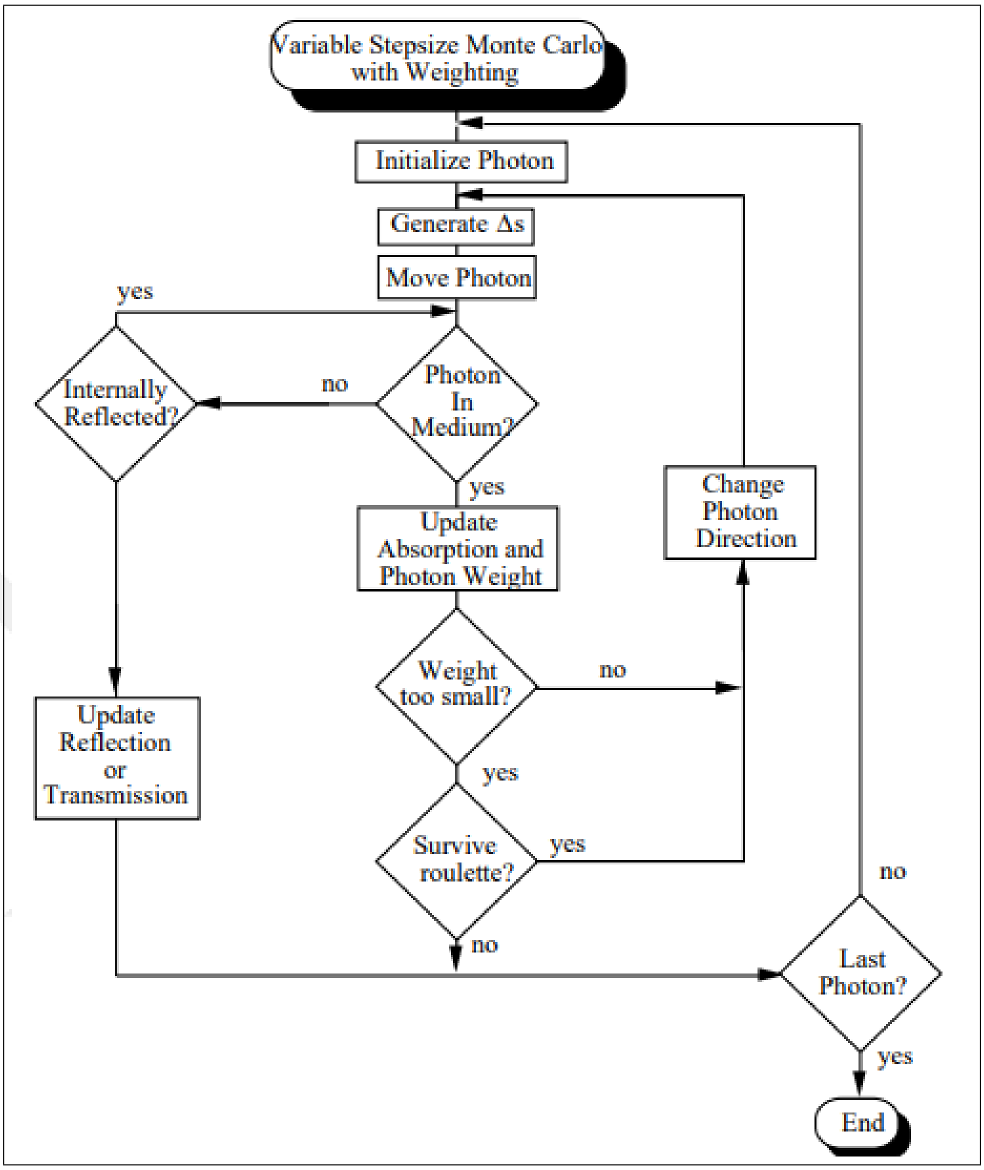

Figure 2.7 Flowchart of a Monte Carlo program [78].

spectra.

3. DESIGN OF A NOVEL REFLECTION SPECTROSCOPY (DRS) MEASUREMENT SYSTEM

Diffuse reflection spectroscopy (DRS) is a well-studied optical technique that can provide a noninvasive and quantitative way of determining the absorption and scattering properties of biological tissues. This chapter presents the development of a new measurement system for DRS in VIS spectral range, 400-700 nm, in order to gather reflectance spectra of a skin tissue. The proposed design in this study utilizes fiber-optic cables coupled with a light source and detectors to transfer the light.

The first part of this chapter gives a literature overview of optic fibers and presents previous research studies done in the field of VIS spectroscopy for the specific application of optic probe design.

The second part describes the methods utilized in this study, including considerations in DRS system design, and introduces the experimental setup. The proposed measurement system is explained in detail together with the descriptions of the light source, detector, and optic probe.

The measurements are demonstrated in the third part. In this part, the derived mathematical equations to obtain an actual reflectance of a target tissue surface are also stated.

In the fourth part, results of the measurements are presented. The hemoglobin spectra obtained from human samples are compared with actual hemoglobin spectra that are well-defined in literature.

In the following fifth section, this study is extensively discussed by describing the significance of the proposed DRS system. In addition, the limitations and future plans are reported.

Lastly, conclusion is given in part 6 and the fields in which the developed system can potentially be used are indicated.

Parts of this chapter were originally a published conference paper titled "Design of a new optic probe for diffuse reflectance spectroscopy" [79]. In this paper, we presented a DRS measurement system with a white LED light source, micro spectrometer and a novel fiber-based optic probe. The proposed system was tested with human subjects and the test results were presented.

3.1 Introduction

Traditionally, designing an optical instrument to be used in clinical studies of DRS has been costly and troublesome either due to the complex detection technologies for data collection, processing, and throughput, or due to the use of high-power light sources, or both [80, 81]. With the improvements in fundamental and applied engineering and electronics, it is now possible to deliver efficient optical energy using low-power light sources and detect the measured signals at high speeds using compact optical spectrometers. Although such compact designs have been demonstrated previously [82, 83], these systems are not suitable for application in our study due to various reasons such as being expensive, laborious to assemble, complex in geometry, and large in size for a portable device.

The main aim of this study was to assemble and validate a small, portable, easy to manufacture and robust DRS measurement system that works in VIS spectral region for quick and routine usage to obtain reflectance spectra. The ease of system setup and the small size of the proposed optic design would make it suitable for use in portable devices.

The most important part of the proposed DRS system is the optic probe that consists of optic fibers. Optic fibers are thin fibers of glass or plastic (e.g., acrylic or polystyrene) that are used to transmit light signals. An optical fiber for spectroscopy consists of a core, a cladding, and an outer jacket. Light transmission is achieved based on the principle of total internal reflection. Total internal reflection is a result of Snell's law for the refraction of light traveling from one medium to another. A typical reflection phenomenon occurring at the boundary of two optically different media with refractive indices n_1 and n_2 can be described as:

$$n_1 sin\theta_1 = n_2 sin\theta_2 \tag{3.1}$$

where θ_1 is the angle of incidence and θ_2 is the angle of refraction.

The light gathering capacity of an optical fibre is considered as numerical aperture (NA). In other words, NA is the sine of the largest angle an incident ray can have for total internal reflectance in the core, which is defined by the difference in the refractive indices of the core and the cladding material. By using Snell's law, NA of an optical fiber with core refractive index n_{core}, cladding refractive index $n_{cladding}$ and acceptance angle α in a media is given by Eq. 3.2

$$NA = n_{media} sin\alpha = (n_{core}^2 - n_{cladding}^2)^{0.5} \tag{3.2}$$

A wide variety of probe designs have been reported in literature to be used in clinical diagnostic application of DRS to measure the emitted light as a function of wavelength [84]. Oblique-incidence illumination and bundle of angled fibers have been used to target soft tissue regions [85, 82]. Variations in fiber size, different source-detector fiber separation, and probe-sample spacing have been shown to influence sensitivity to different layers in tissue [86]. The intensity of reflected light is strongly dependent on the source-detector geometry. In other words, the arrangement of the source and detector optic fibers affects the number of reflected photons obtained. Therefore, fiber-optic probe design has an important role in obtaining spectroscopic information. The depth that the photons reach in the tissue is also affected by the arrangement of the source and detector fibers. The depth is clinically important because it is necessary to gather the reflected photons that are scattered from the site where the target chromophores exist. As the source-detector separation increases, the obtained spectra originates from the deeper tissue.

3.2 Methods

3.2.1 Considerations in DRS System Design

Firstly, optical fibers, when used for collection of the emitted light, can detect a relatively small portion of the reflected signal; thus, high-quantum-efficiency, low-noise detectors are required to gather the reflected spectra. A spectrometer, an optical device for measuring the amount of reflected light, is an ideal optical instrument to be used in DRS due to its aforementioned properties. The size and design of a spectrometer have a strong effect on the spectral resolution and the range of working wavelengths. These properties are inversely related to each other, that is, as the spectral resolution increases, the wavelength range decreases or size increases and vice versa [87]. State-of-the-art spectrometers are available in compact size that is ideal for clinical applications, particularly transcutaneous bilirubinometry. Most systems interface with computers via USB for power supply. However, in this design, a battery-powered system is needed since a portable device is proposed. Therefore, low-power consumption of the device becomes an important consideration in spectrometer selection.

Secondly, selection of the light source for a DRS system has to be considered. It is essentially selected based on its brightness and wavelength range. The brightness, or power output, of a light source must be high enough so that the reflected signal is sufficiently higher than the background noise signal. Additionally, the measurement timescale (integration time) should be in a reasonable range that can be accomplished by selecting a light source with enough output power. However, this power should be limited with the level of maximum allowable power of the light incident on the tissue in DRS *in vivo* so as not to damage the tissue under test. In some applications, such as transcutaneous bilirubinometry, fast integration time is required to decrease the environmental noise effects such as motion blur. Thus, achieving shorter integration time is one of the most vital issues in DRS [87, 88].

Another aspect that should be taken into consideration in the selection of a light source is the wavelength range of the selected light [88]. It should cover the wavelength range of the reflectance of the target chromophores. Coherent light sources, such as lasers diodes, can illuminate the tissue with higher power than white-light arc lamp or light emitting diode (LED) sources, but they do not span the entire VIS spectrum where the reflectance spectra of melanin, hemoglobin and bilirubin are observed. A broadband light source whose illumination includes the most diagnostically relevant wavelengths in transcutaneous bilirubinometry should be selected. For this kind of light sources, it is important to ensure that the whole relevant part of the wavelength is transmitted to the target tissue in order to prevent dispersion effects.

Optic probe design is another major component of a DRS system. Traditionally, the appliance used to measure diffuse reflectance is an integrating sphere [59]. Because of its geometry, the integrating sphere has the ability to collect most of the reflected light, remove any directional preferences, and present an integrated signal to the detector. However, for a portable measuring device, application of DRS necessitates being compact, lightweight, small-sized, and having user friendly optical apparatus. Integrating sphere structure does not allow miniaturization, and hence, is not suitable to be used in a portable device. Currently, fiber-optic probes with varying diameters and fiber cable arrangements are being used in optical probes. The degree of tissue penetration depth and the angle of interface with tissue surface can be determined by the fiber probe geometry. Illumination and signal collection can be accomplished either with a single optic fiber or a bundle of fibers. There are numerous fiber-optic probe designs in literature such as the construction of a probe with linear alignment of fibers, placing the detection fibers in different places, and a circular fiber arrangement with a source fiber in the middle of all other fibers [89]. Also, it is possible to face a micro-machined fiber-optical sensor with different number of source fibers and numerous collection fibers [90]. Alejandro et al. designed an oblique incidence DRS by placing the source fibers obliquely with the angle of 45^0, 25^0, and perpendicular to the tissue surface. In that design, the distance between source and collection fibers is 1 mm. They used 5 source and 20 collection fibers in their design [91] as depicted in Figure 3.1.

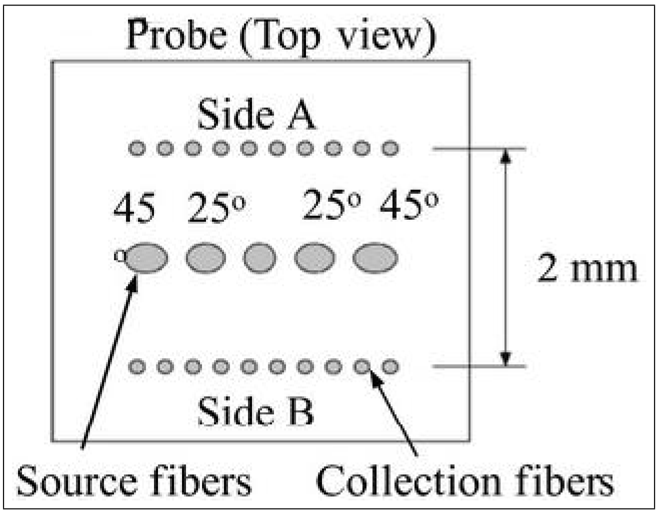

Figure 3.1 Oblique incidence light optic fiber design [91].

Despite the wide use of fiber-optic probes, their manufacturing process is rather complex. Especially, while making a custom-designed probe, one may need to cut the fibers, which is not an easy process. Cutting the fibers needs special cutter devices and after the cutting process fibers' endings need to be polished, which is another difficult and time-consuming process. Furthermore, arranging fibers in a desired alignment for making fiber bundles is not easy because of small diameters. In a design that is proposed for use in transcutaneous bilirubinometry, one should consider designing the optic probe with a compact size, easy to be manufactured and assembled, and efficient in terms of light transmission. Using multi-mode optic fibers rather than single-mode ones seems to be advantageous because of their larger size and higher NA values. Circular arrangement of optic fibers makes the design smaller in size.

Another important property that an optic probe should have is the ability to collect the returning light from deep within the tissue. As mentioned in previous sections, reflected light includes two main components: specular reflectance and diffuse reflectance. The diffuse component of the reflected light is desirable, and even essential, if the reflectance spectroscopy is used for examining the subcutaneous tissue, since specular reflectance component contains information only about the surface of the skin. Information about the presence or concentration of a chromophore, such as hemoglobin and bilirubin, in the subcutaneous tissue is carried by diffusely reflected light from the human tissue. The epidermis layer has very little or no blood, and thus, corresponding diffusely reflected light component from epidermis layer contains little or no biological information. Consequently, it is critical to collect only diffusely reflected light returning from the subcutaneous tissue.

Diffuse reflectance spectrum carries information about the concentration of the biological chromophores deep inside the human skin. It is critical to acquire sufficient reflected light intensity to be able to calculate the concentration of those chromophores. In order to attain this sufficient intensity, integration time or efficiency of the system can be increased. However, in some applications, such as transcutaneous bilirubinometry, fast integration time is required to decrease the environmental noise effects such as motion blur. Thus, achieving shorter integration time is one of the most vital issues in diffuse reflectance spectroscopy. Increasing the light transmission efficiency is a means to shorten the integration time. For better light transmission efficiency, light delivery path should be coupled to the light source effectively and so should the light collection path to the detector.

3.2.2 Proposed DRS System

The proposed DRS measurement device in this study comprises three main components including a light source to illuminate the skin, a light transmission probe to deliver the incident light and to collect the reflected light, and a spectrometer to evaluate the obtained reflected light. With the help of a processing unit, the measurement results (raw spectra) are processed and analysed for predicting the concentration of the chromophores such as hemoglobin, bilirubin or melanin. The block diagram of the proposed system is shown in Figure 3.2.

Light source of the proposed design is a key component which was selected primarily on the basis of its wavelength range. Light absorption of bilirubin, hemoglobin and melanin are wavelength dependent with characteristic variations in VIS range between 400 nm and 700 nm. The proposed approach benefits from these characteristic

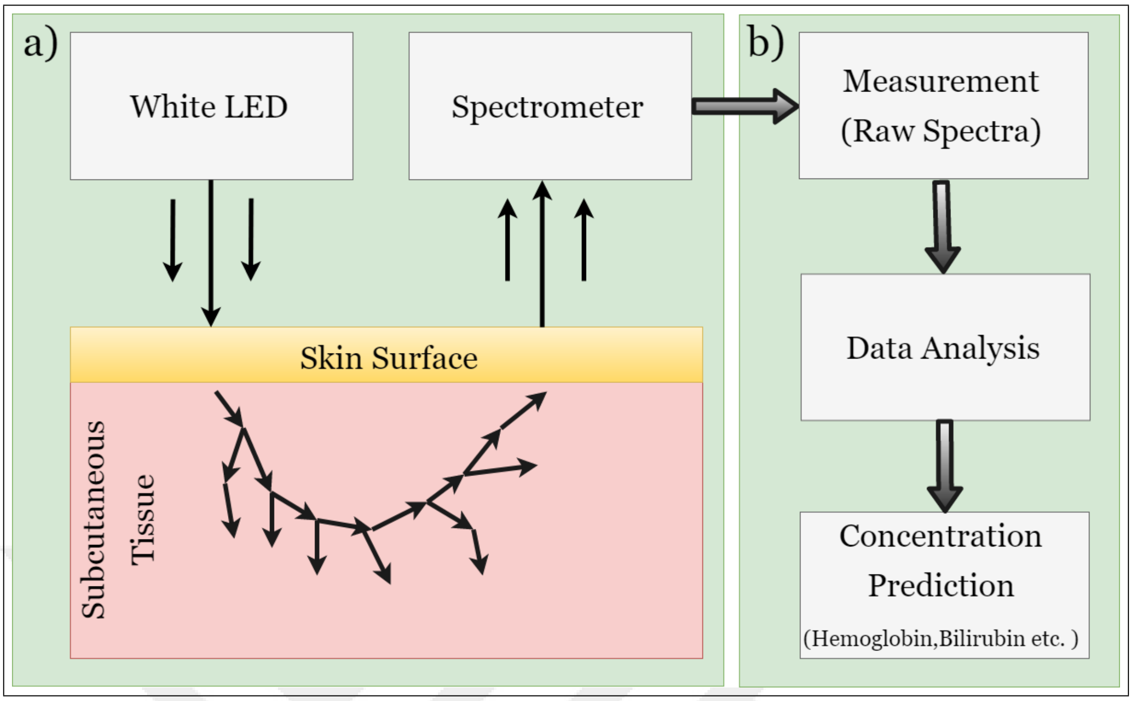

Figure 3.2 Block diagram of the diffuse reflectance measurement setup. a) A white LED illuminates the skin surface, and the spectrum of the reflected light is measured with the help of a spectrometer. b) Data analysis and chromophores (bilirubin, hemoglobin, etc.) concentration prediction are done by using the output data of the spectrometer.

responses of the three substances while separating their concentrations in the subject. To this end, the whole range of VIS is scanned to cover the concentration-sensitive range for all three blood substances. To be able to acquire data reliably in a single pass, it is better to have a light source which has non-zero emission power over the entire VIS. Therefore, a white LED was chosen as the light source due to its broad spectrum range, and its 1 Watt output provided sufficient power in all wavelengths of interest. The chosen LED was assembled on an in-house developed electronic LED module and triggered with a switch button.

The second key component is the detector. A fingertip-sized spectrometer (C12666MA) from the Hamamatsu Inc. was used as a detector because of its convenience for portable devices. The sizes are 20.1x12.5x10.1 mm. The compact size is not the only advantage of C12666MA, but its low power consumption (30 mW) also makes it advantageous for a portable device. The spectral response range is 340 to 780 nm, which is ideal for this study. It takes 256 samples in VIS with a spectral resolution of 15 nm. High-sensitivity complementary metal–oxide semiconductor (CMOS) linear image sensor technology gives it high quantum efficiencies, enables short integration times and sufficient spectral resolution [92].

The last key component, but probably the most important one, is the optical probe, and therefore, its design will be described in more detail in the following subsection.

3.2.3 Proposed Optic Probe

In the design of the proposed optical probe, it was intended to use two independent optical paths. One is for illuminating the tissue surface and the other is for collecting the diffusely reflected light from the subcutaneous tissue. Symbolic representation of the proposed optical probe design and tissue interaction can be seen in Figure 3.3. This figure illustrates the concept of this new optical fiber probe for DRS measurements *in vivo*. The collection fibers are located symmetrically relative to the excitation fibers in a circular arrangement.

The proposed optical probe is designed with multi-mode optic fibers. In order to increase the light transmission capacity of the optic probe, optic fibers with larger core diameters and higher NA values are chosen. The chosen optic fibers have the core diameter of 750 μm and 0.39 NA value. 19 optic fibers are used in the proposed design as shown in Figure 3.4.

The outer 12 optic fibers are coupled with the white LED and enable the transmission of the generated light to the tissue site of interest. The inner 7 optic fibers gather the light that is reflected from the subcutaneous tissue and transfer it to the spectrometer. The effective coupling of these 7 optic fibers with the slit of the spectrometer is vital in order to collect all the reflected photons. Therefore, a tubular head is designed to hold the optic fibers as a bundle, see Figure 3.5.

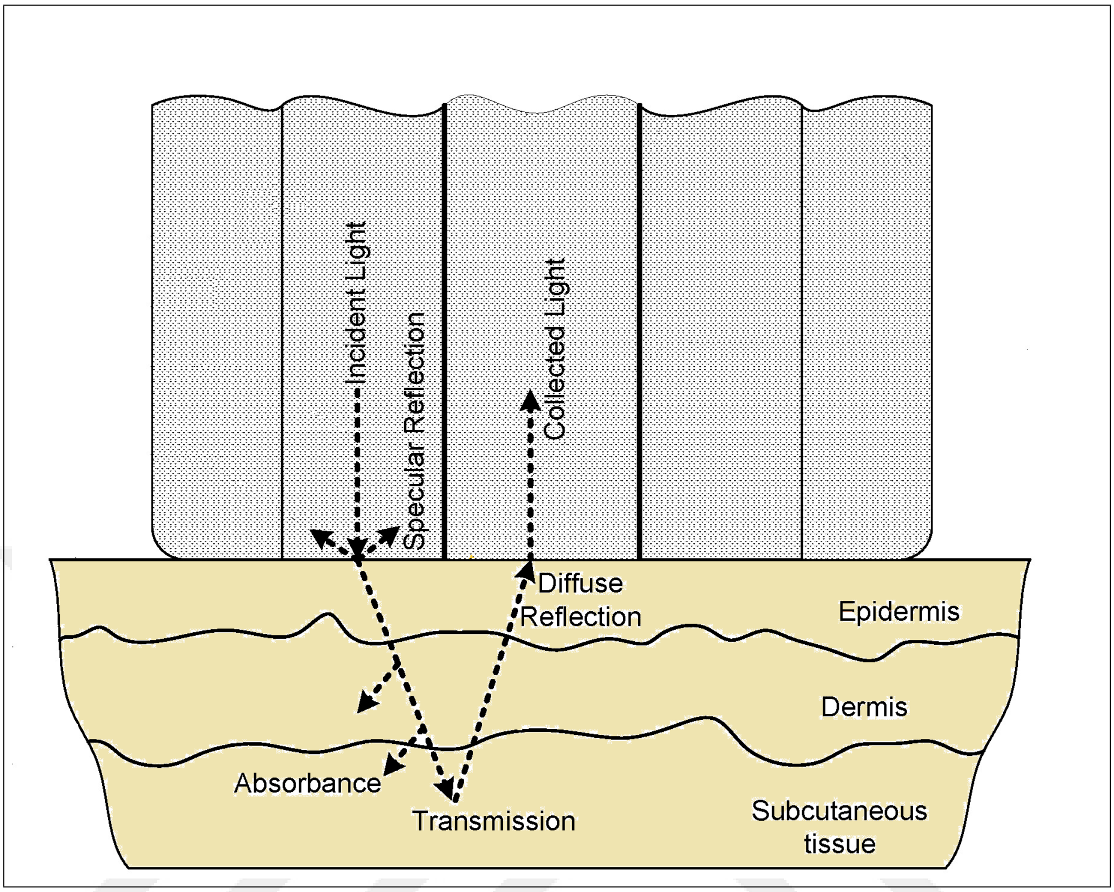

Figure 3.3 Cross-section view of the proposed optic probe and symbolic representation of the proposed optical probe design and tissue interaction.

The optic fibers responsible for the illumination of the tissue are coupled with the white LED via LED holder as depicted in Figure 3.6. Inner surface of the LED holder is mirrored in order to increase light transmission efficiency.

Both the collection and transmission optic fiber bundles are glued together in order to keep the arrangement of the fibers. All of the polishing process was done manually according to the guidelines produced by Thorlabs Inc.[93]. Firstly, we used a polishing film with a diameter of 5 μm. Placing 3 or 4 drops of water on the polishing film helps the removal of the particles. Polishing was done by applying the proper pressure to the optical fibers and drawing a figure eight pattern. Then, 3 μm and 1 μm polishing films were used and the same processes were performed again. Approximately 15 repetitions of the figure eight was enough for each step. After these repeated processes, the optical fibers were wiped with isopropyl alcohol solution. The success of

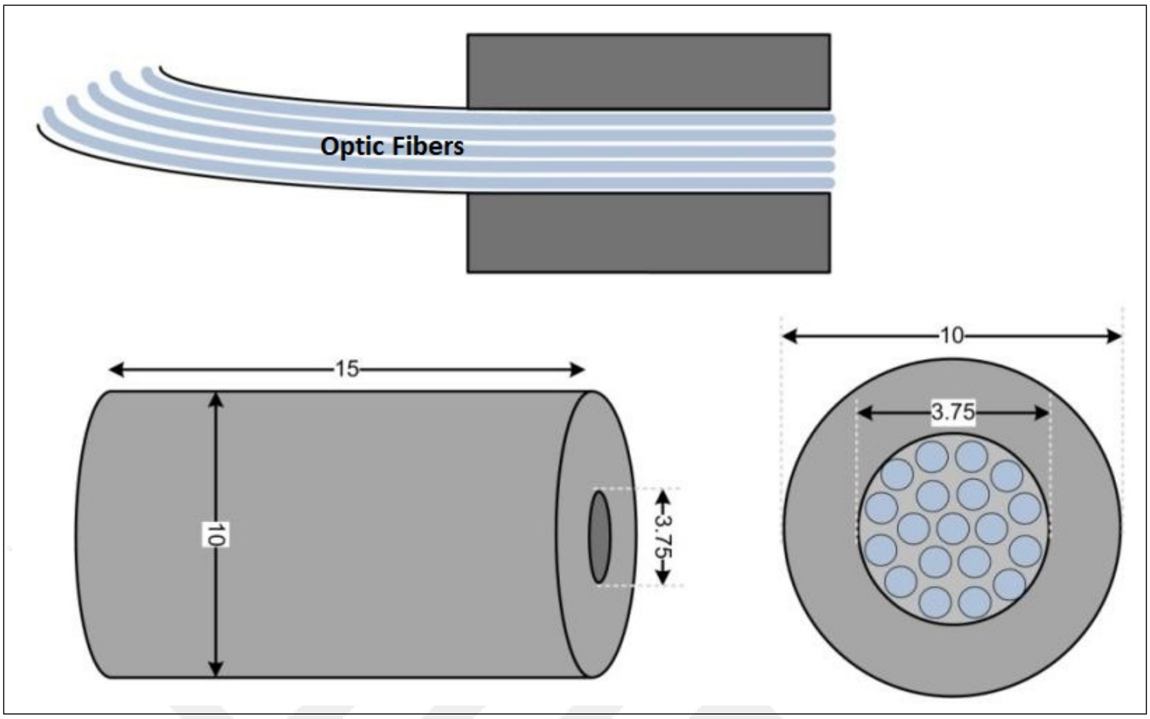

Figure 3.4 Proposed optic probe. 19 optic fibers with a core diameter of 750 μm are used in the proposed design. All given numerical dimension are in mm. The optic fibers are bundled in a tubular head. The head diameters are 15x10 mm.

the polishing process was controlled by a microscope. If the optic fibers failed to pass the final inspection, the polishing with the 1 μm polishing film was repeated.

In general, collection and illumination channels are exchangeable. Therefore, because of its simplicity to test, we made all optic fibers illuminators and checked whether they were properly aligned. As seen in Figure 3.7, the optical fibers are arranged perfectly with the help of a fiber cover.

3.3 Measurements

The proposed DRS system is tested in order to ensure that it can be used in a DRS measurement device. While designing this system, it was aimed to develop a device for gathering the spectra of the subcutaneous tissue. Before using this system, some measurements such as dark measurements and reference measurements had to be made.

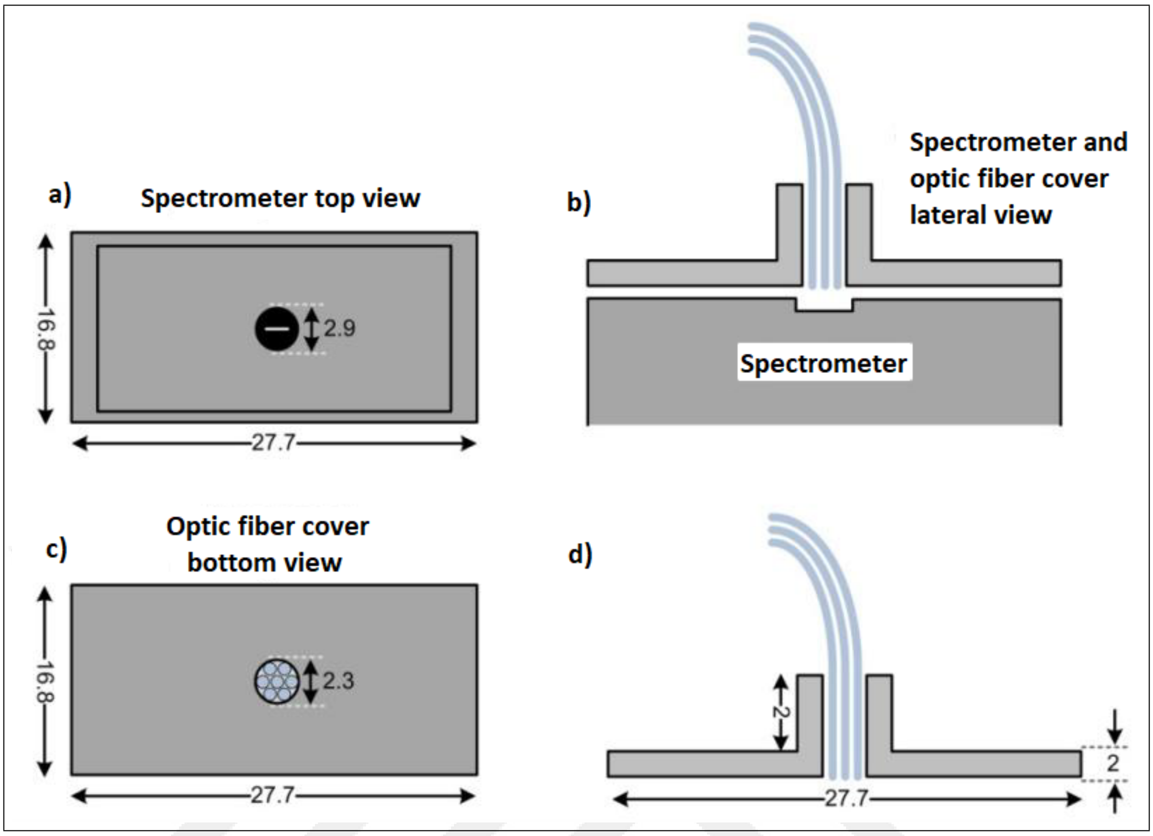

Figure 3.5 Optic fibers and spectrometer coupling. All given numerical dimension are in mm. a) Top view of the spectrometer. b) Lateral view of the spectrometer and the optic fiber cover. c) Bottom view of the optic fiber cover. d) Optic fiber cover with dimensions of 27.7x2 mm.

Dark measurement: A measured spectrum contains a baseline which originates from a voltage that is added to the original signal. Often it is desirable to subtract a dark spectrum from a measured spectrum. In practice, this requires two measurements. The first one is taken with the light source on and the second one is taken with the light source off. In this section, we denote the dark measurement spectrum as $N(s)$.

Reference measurement: This kind of measurement is done with a white reference sample to calibrate the setup for 100% reflection. However, there is no 100% reflective material in the real world. Generally, a ceramic surface is an ideal option for taking reference measurements due to its high reflection capability and rigid optical properties that change insignificantly over time, if at all. By taking a reference measurement, it becomes possible to obtain a spectrum which contains the effects of the light source, the optical paths, and the detector. We denote this spectrum as $H(s)$.

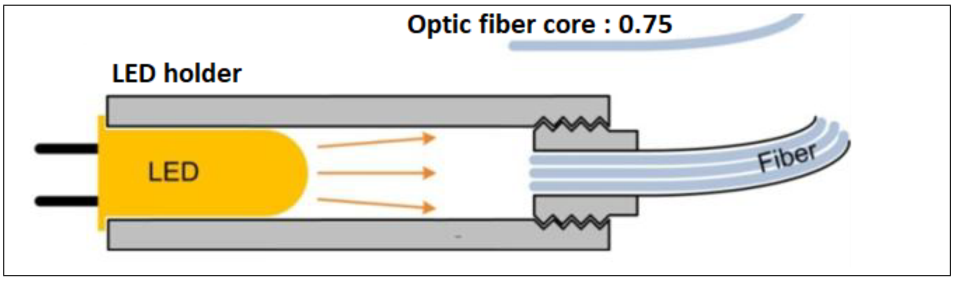

Figure 3.6 Optic fibers and LED coupling. All given numerical dimension are in mm. LED holder fixes the LED and enables coupling of optic fibers and LED. Inner surface of the LED holder is mirrored in order to increase light transmission efficiency.

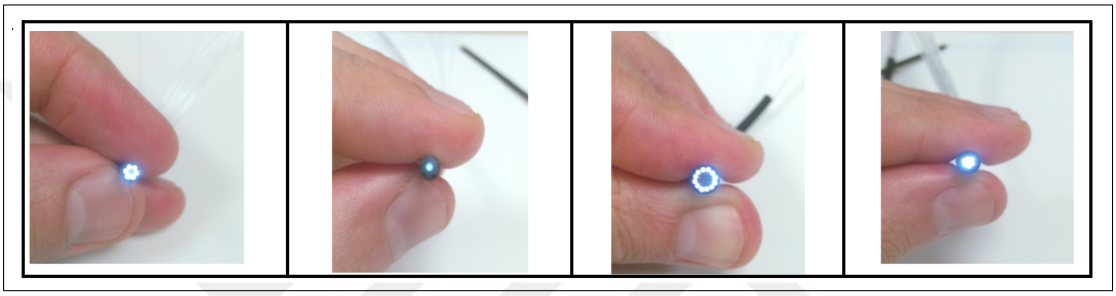

Figure 3.7 Optic fiber bundle testing. To check the optic fiber arrangement of the bundle, all the fibers are tested as if they are illuminators. It is seen that both transmission and collection optical fibers are arranged properly.

If we denote the spectra that are obtained by each surface measurement as $M(s)$ and the actual surface spectra as $D(s)$, one can realize that $M(s)$ spectra are actually a combination of $D(s)$, $H(s)$, and $N(s)$. This relationship can be defined mathematically as in Eq. 3.3.

$$M(s) = D(s).H(s) + N(s) \tag{3.3}$$

Consequently, in order to obtain the actual reflectance spectrum of a surface, the following basic mathematical model should be applied to all the taken reflectance measurements.

$$D(s) = \frac{M(s) - N(s)}{H(s)} \tag{3.4}$$

3.4 Results

With the help of the mathematical derivation in Eq. 3.4, it was aimed to obtain hemoglobin spectra, which is well defined in literature [94]. The melanin pigment, which is abundant in the epidermal layer, acts as an attenuating filter and affects the hemoglobin spectra. However, skin in our palms has less melanin pigmentation than other parts of the body and this attribute makes palms an ideal site for hemoglobin spectrum measurements with minimal melanin effect. The obtained reflectance spectra from three people with different hemoglobin levels are shown in Figure 3.9.

The measurements were taken with 100 ms integration time. The reflected light from the palms was gathered with the proposed optic probe. The obtained spectra were converted to electronic signals with the help of an analog to digital converter (ADC). Then they were transferred to the processing unit as digital signals. In the processing unit Eq. 3.4 was applied and the actual spectra of the palms were obtained. These spectra were drawn in a graphical user interface (GUI) written in c# programming language as shown in Appendix.A. As seen in Figure 3.9, the obtained hemoglobin spectra have peaks at around 414, 542 and 576 nm wavelength as the theoretical hemoglobin spectrum has (See Figure 3.8).

These obtained spectra were compared with the theoretical hemoglobin spectrum shown in Figure 3.8. One can see that the measurement results are remarkably similar with the actual hemoglobin spectrum. They have peak values at the same wavelength points. Also, it can be observed that the obtained spectra have similarly shaped signals in the range 500 and 580 nm, where hemoglobin has dominant absorption capability.

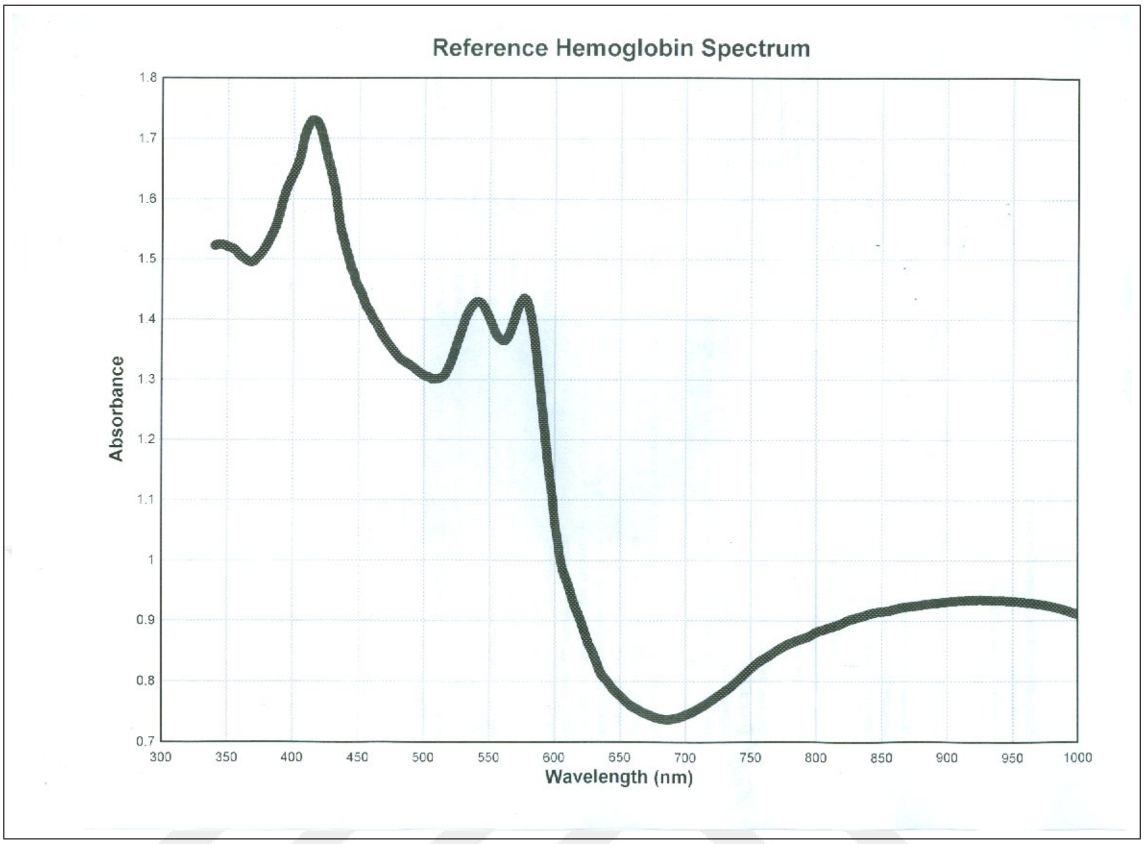

Figure 3.8 The theoretical reference spectrum for hemoglobin. Peaks occur at 414, 542 and 576 nm, respectively [94].

3.5 Discussion

Previous reports have documented the potential of reflectance spectroscopy for noninvasive diagnosis in clinical studies. The DRS system described in this report allows *in vivo* measurements of tissue diffuse reflectance spectra to determine the concentration of chromophores such as melanin, hemoglobin and bilirubin. With this proposed design, it was aimed to obtain a DRS measurement system that is affordable, easy to manufacture, and applicable to portable devices. The proposed design does not have an advanced optic probe that brings complicated geometry and difficulties into the manufacturing process, but has sufficient illumination and collection efficiency. Also, instead of using a spectrometer with high resolution but larger in size, we have chosen a compact spectrometer with moderate resolution. In addition, we aimed to benefit from the usage of LEDs as a light source for the ease of driving electronically. According to the test results, we have reached our goals in our study.

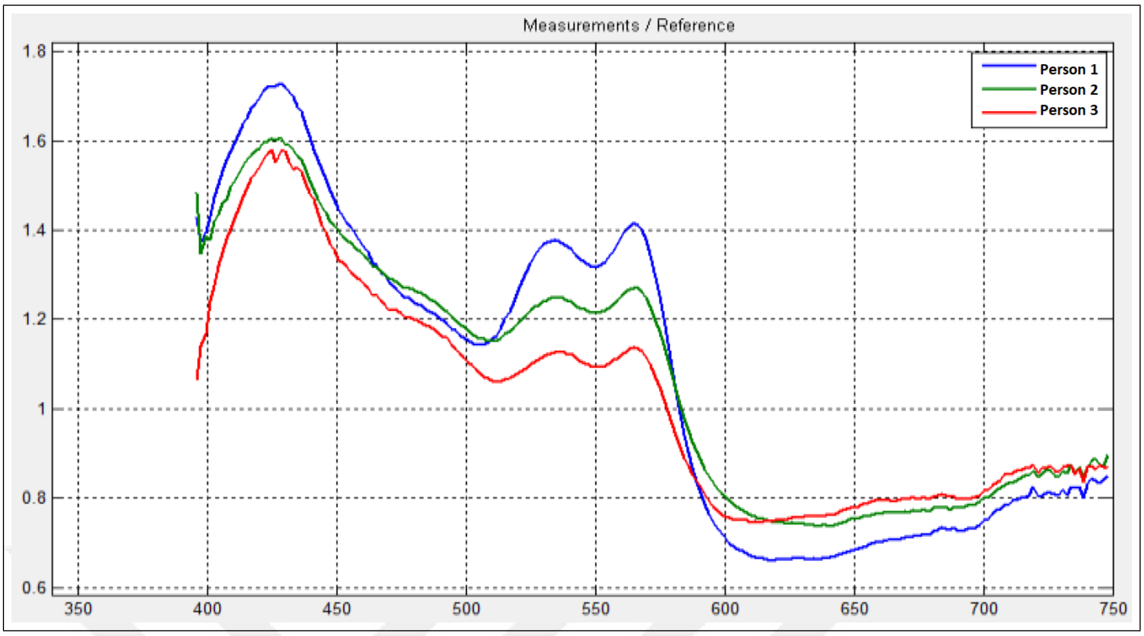

Figure 3.9 Measured diffuse reflectance spectra from 3 human samples. Peaks occur at 414, 542 and 576 nm, respectively [94].

One of the major considerations that have to be taken into account when designing and building the optic probe is the sampling depth of the DRS probe, which is defined as the depth reached by 50% of the incident photons. This depth is affected by different factors, such as the optical properties of the target tissue, the geometry of the optic probe, and the wavelength of the light [95]. Distance between the source and collection fibers should be small in order to minimize collection of multiply scattered light and to maximize collection of light that is coming from the subcutaneous tissue. Hennessy et al. investigated the effect of distance between source and detector on the sampling depth by using Monte Carlo model [95]. They found that with the source-detector distance of 0.25 and 1 mm, it was possible to measure sampling depths of up to 0.3 and 0.7 mm, respectively. If someone wants to measure larger sampling depths, the source-detector distance should be increased. They also indicated that the sampling depth was wavelength-dependent. In VIS, the sampling depth varied in the range of 0.4 to 0.7 for a distance of 1 mm between source and detector. In light of their valuable findings, we have chosen optic fibers with a core diameter of 750 μm, which enables source-detector separation with a distance of 750 μm to measure sampling depth up to 750 μm. This depth is exactly what we want to achieve in this study, since the chromophores that we want to measure are found at this depth of the tissue.

Another major consideration that we have to take into account is NA of the optic fibers. According to recent studies, fiber-based optic probes have limited collection efficiency for two reasons. The first reason is that the cylindrical fiber cores are surrounded by noncollecting fiber cladding layers, in other words, they contain dead areas, which prevent photon collection. The second reason is that the low NA of optic fibers (typical optic fiber NA = 0.22 [96]) [67] limits the acceptance angle of the reflected light. Replacing collection fibers with high photo diode, which has typically 0.95 NA [97], improves the reflectance collection efficiency [98] and leads to improvement in SNR [67]. However, using photo diodes in this study is not feasible since it was aimed to design a compact and easy to manufacture DRS system. To overcome the aforementioned problems, we used a multi-mode optic fiber with 0.49 NA with larger core diameter (750 μm). Additionally, since the collection and illumination fibers are lined up on a circle, the fiber claddings act as a separator between source and detector, which is a requirement for DRS measurement system (source-detector distance).

Designing a DRS measurement system with fiber-optic probes are simple and inexpensive; however, they are applied by contacting the tissue, which might lead to variations because the applied pressure affects the local blood content in the tissue [99]. Here, in order to handle this problem, a limit switch is implemented in the proposed design. This limit switch triggers the system and initiates the measurement when an appropriate pressure is applied. With the help of this system, we were assured that we applied the same pressure to the skin surface in each measurement and prevented the variations in local blood content in the tissue.

The optic fibers used in this study were selected with a biomedical application in mind. Therefore, the probe tip in contact with the tissue surface should be analyzed for potential hazards before being used in clinical studies. An analysis of possible risks and protection against those risks is a prerequisite of human subject studies supported by the National Institutes of Health (NIH). A guidance document that was released by the US Food and Drug Administration (FDA) [100] can also be helpful for the evaluation of hazards of fiber-optic probes. Likely adverse events that may result from the use of fiber-optic probes are optical radiation hazards, thermal hazards, electrical shock hazards, clinical hazards (transmission of diseases), and material toxicity hazards [101]. According to a general evaluation of medical devices, transmission of diseases is the most common adverse effect of fiber-optic probes, and their materials should be tested for cytotoxicity, sensitization, irritation, and, depending on the application, for acute systemic toxicity [101]. In this study, the optic probe contacts only with the tissue surface. Thus, we focus on eliminating the adverse effects caused by transmission of diseases. To cope with this hazard, we cleaned up the optic tip with an alcohol-based solution before each application. Also, we ascertained that we have not used an optic fiber made of cytotoxic material. Lastly, since our optic fibers are made of acrylic material, which is a good electric isolator, there was no risk of electric shock.

For spectroscopic applications, multi-mode fibers with core diameters of 50 to 1000 μm are usually used. Short pieces (up to 2 m) of fibers with larger core diameters can be produced in custom runs. Therefore, in our study, it was not possible to find an optic fiber in the length of 10 to 20 cm in the market. By using a fiber-optic cutter, we cut the fibers into small pieces to fit the design. After cutting the optic fibers, they were polished as described in detail in the previous sections.

The working principle of the optic fibers depends on guiding the light down the fiber core due to the difference between the indexes of refraction of the core and the cladding. Additional coating is applied by using a flexible buffer material to preserve the fiber core; however, it is hard to bend the fiber without causing microscopic cracks [102]. The challenge that we faced in our design was not to bend the optic fiber with an angle greater than the allowable bending radius. In case of a higher bending angle of the optic fibers, microscopic cracks may result and also light may exit the core and hit the jacket, which in turn leads to a decrease in light transmission efficiency.

Light source stability is a vital issue for a proper measurement. For assessment of the light source stability, the illumination power out of the LED was monitored by measuring the current consumption of the system. As the acquisition period increases, the temperature increases and causes variation in the spectra of the LEDs. Therefore, the integration time was kept shorter at 100 ms and acquisition of another measurement before 1 second elapsed was prevented. Thus, increasing the temperature of the LED light source was avoided.

In case of a small wavelength range, a light source whose illumination includes the most diagnostically relevant wavelengths for a particular application should be selected. On the other hand, for broadband light sources, it is important to ensure that all the included wavelength components are transmitted satisfactorily through the optical system, avoiding dispersion effects. The white LED used in this study has a flat spectrum in VIS, enabling us to obtain a spectrum from the illuminated tissue surface that covers all the wavelength range from 400 to 700 nm.

For better light transmission efficiency, light delivery path should be coupled to the light source effectively and so should the light collection path to the detector. To ensure optimal coupling, the end of the optic fiber cable is polished. If the exit surface is polished with an oblique angle with respect to the fiber axis, the output will be deflected and thus leads to a decrease in light transmission efficiency. Along with the polishing process, it is also very important to properly align the fibers with the spectrometer slit. Since the spectrometer used in this study (C12666MA) has a small slit aperture (50 x 750 μm), care should be taken in coupling the collection fibers with the spectrometer.

Although our results are promising and in agreement with the studies conducted earlier on hemoglobin spectrum, lack of numerical comparison is a limitation of this study. We should measure the hemoglobin level quantitatively just before the measurements are taken from each subject. Quantitative measurements in a clinical study are planned for future studies.

3.6 Conclusion

This chapter presents the development of a DRS measurement system to be used in a portable device. The proposed system was designed to be compact, cheap, and easy to manufacture. These desired features were kept in mind while designing the optic probe and selecting the light source and the detector.

Firstly, a novel optic probe, which consists of 19 optic fibers with core diameter of 750 μm, was designed in this study. 12 of the optic fibers, which were placed in the outer side of the probe tip, were used to illuminate the tissue surface. The remaining 7 optic fibers were responsible for the collection of the diffusely reflected light and transmission this light to the spectrometer. Secondly, using a white LED as a light source was advantageous since it is easy to drive it electronically and have a spectrum in all VIS wavelengths. Lastly, a compact spectrometer from Hamamatsu Inc. was used as a detector because of its small size.

The performance of the designed DRS measurement system was tested using human samples. Hemoglobin spectra were used for evaluation. Thus, diffuse reflectance measurements were taken from the palms of human subjects, where it is optimal to obtain hemoglobin spectra. The obtained spectra of the palms were compared with the actual hemoglobin spectra taken from the literature. The findings presented here suggest that the proposed DRS measurement system is very promising for usage in *in vivo* measurements.

These findings indicate that the proposed DRS system has a potential to help us determine the concentration levels of chromophores such as melanin, hemoglobin and bilirubin, with a proper detection algorithm. In the following chapter of this dissertation, determining the concentration of bilirubin pigment with a suitable detection algorithm was aimed. Here, the main purpose is to use this system for the detection of neonatal jaundice.

4. NEWBORN JAUNDICE DETERMINATION BY REFLECTANCE SPECTROSCOPY USING REGRESSION METHODS

Diffuse reflectance spectroscopy is a non-destructive and rapid method to obtain biochemical and physiological information by investigating the optical properties of skin. Transcutaneous bilirubin (TcB) measurement utilizes reflectance spectroscopy to determine the jaundice level in newborns. Although TcB measurement has some advantages over total serum bilirubin (TSB) measurement such as being noninvasive, noninfectious, painless, and instantaneous, the existing TcB devices cannot yet replace TSB devices due to the inaccuracy of measurements. In this chapter, we propose the use of reflectance spectroscopy in conjunction with regression tools such as multiple polynomial regression (MPR), artificial neural network (ANN), and support vector regression (SVR) to predict the jaundice level. The proposed methods were tested on TcB measurement data obtained from 314 babies. TcB measurements were collected by two devices; a commercially available product, Draeger JM-103, and a prototype device on which we implemented the proposed algorithms. The results are encouraging towards increasing the clinical usage of transcutaneous bilirubinometers as all the three methods accurately predict the jaundice level with a correlation value between 0.932 and 0.943. The proposed use of ANN improves the noninvasive transcutaneous approach, with results converging to more accurate invasive serum bilirubin measurements by blood sampling.

The first part of this chapter gives a brief description of the fitting procedure and a literature overview of the nonlinear fitting methods, MPR, ANN, and SVR, that we studied in this dissertation.

The second part gives an account of the methodology of this study including the description of the prototype device used, data collection procedure, and pre-processing of the obtained data. Monte Carlo simulations of the newborn skin, calibration of the device used, effects of melanin and hemoglobin pigments on bilirubin absorption spectra, and data analysis procedure are also described.

The fitting procedure including the application of MPR, ANN, and SVR methods are described together with the explanations of parameter selection and mathematical expressions in the third part.

In the fourth part, results and analysis of the study are presented. The results obtained from the three applied methods and Draeger JM-103 are compared.

In the following section, the fifth part, this study is extensively discussed by elaborating on the significance of the proposed methods.

In the last part, conclusion is given by summarizing the main points of this study. Future plans are also presented.

Parts of this chapter were originally a published journal paper titled "Newborn jaundice determination by reflectance spectroscopy using multiple polynomial regression, neural network, and support vector regression" [103] and a published conference paper titled "Determination of newborn jaundice level by transcutaneous bilirubin measurement" [104]. The topics covered by the papers are described in more detail in this chapter.

4.1 Introduction

Fitting procedure involves inverse methods that consist of defining a mathematical model of the acquisition process and numerical methods that illustrate the relationship between the optical properties and the obtained diffuse reflectance spectra. Inverse methods aim to find the best fit between the extracted optical properties of the tissue and the measured reflectance spectra. Numerous approaches such as multivariate regression analysis, partial least squares (PLS), principal component analysis

(PCA), spline interpolation, and perturbation theory can be used to find the best fit parameters [105, 106].

Creating calibration curves is an application of inverse methods. They are generally used for quantitative analysis in spectroscopy to determine the concentration of chemicals in samples. Commonly, the concentration of the analyte, the chemical being measured, is the independent variable and is plotted on the x-axis. The detector response, the measured spectrum, is the dependent variable and is plotted on the y-axis. A calibration curve is obtained by plotting the known concentration of chemicals in any tissue versus the detector response. While making a calibration curve for spectroscopic data analysis, it is effective to use multivariate data, which leads to a robust and precise method less sensitive to spectral artifacts. Multivariate methods that find the relationship between the independent variables (predictors) and the dependent variables (response) are generally called regression methods. Linear regression methods are used when the measured spectrum is linearly dependent on the properties of the chemical concentration or composition. However, this approach is not appropriate in some instances, such as jaundice level determination from the skin surface since the bilirubin concentration in the extravascular region is not linearly correlated with the concentration in the blood due to the limited volume of the extravascular region [9].

One method that can be used for nonlinear fitting purposes is nonlinear polynomial regression, in other words multiple polynomial regression, with a second or higher degree. MPR uses multiple independent variables to provide parameter estimation based on the least squares approach similar to linear polynomial regression. Unfortunately, unlike linear regression, there is no explicit mathematical solution and special algorithms are required to minimize the error by iterative numerical approximations [107]. Moreover, one should note that generalizing the optimization or minimization is not always a straight forward process for such models because of the nonlinear relationship between parameters [108]. Multicollinearity and overfitting are two main problems in multiple regression methods. The former arises when two or more predictors are correlated with each other and the latter occurs if there are more predictors than needed to model the regression [109, 110].

The improvements in modern applied mathematics and advancement of computing power led to a wide variety of nonlinear machine learning methods. Among these approaches, ANN is the most effective and popular [111]. They have been used for modeling complex relationships between inputs and outputs producing breakthrough results in recent years [112]. Although the main applications of neural networks are in speech recognition [113, 114], pattern recognition [115, 116], customer review sentence sentiment classification [117], and 3D human poses recovery [118, 119], etc, neural network methods have been found to be useful alternatives to statistical techniques such as those that involve regression analysis [120, 121]. Multilayer feed-forward neural network, trained with a back-propagation learning algorithm is based on the supervised procedure, i.e., the network constructs a model based on examples of data with known output.

Support vector machines (SVM) might also be regarded as a promising methodology that can be applied for spectral regression purposes. SVM is an n-dimensional vector that divides data into two optimal hyperplanes. SVM models are closely related to ANNs; a SVM model with a sigmoid kernel function is very similar to two-layer feed-forward ANN. SVM-based techniques are advantageous in modelling nonlinear relationships [122, **?**, 123]. Also, SVM can be used in classification and regression problems. SVR is the application of SVM to the case of regression [124]. The basic principle of SVR is the same as that of SVM for classification, with only a few minor differences. The main purpose of SVR is finding a function with at most ϵ-deviation from the target value. SVR is capable of solving nonlinear problems relatively faster and is more advantageous in dealing with high dimensional input vectors compared to the ANN [125, 126]. Also, SVR needs fewer training data during the learning process for a better regression and is capable of solving overfitting problems. For a more detailed description of SVM and SVR Vapnik [124], Scholkopf and Smola [127], and Cristianini and Shawe-Taylor [128] may be consulted.

This chapter aims to design fitting algorithms by employing the most used and aforementioned nonlinear approaches MPR, ANN, and SVR. These three fitting algorithms are compared by evaluating their predictive performance in determining the jaundice level in newborns. All the input data used by the fitting methods were obtained from 314 newborn babies in a neonatal intensive care unit by using a prototype TcB measurement device. While the measured spectrum values were used as input variables in the prediction algorithms, TSB results were used as output variables to train and test the algorithms. The prediction results of those three methods are compared with TSB values by calculating the correlation coefficients (r), mean absolute error (MAE), and bias. We also compare the predicted results with the measured results of Draeger JM-103 which is a commonly used commercially available TcB measurement device.

4.2 Methodology

4.2.1 Measurement Setup (Prototype Device)

The TcB measurements are obtained with a handheld, battery-powered prototype device for investigating the optical properties of tissue by reflectance spectroscopy. This prototype device can be examined in two ways: optically and electronically.

In optical examination, the typical measurement setup comprising three main components as depicted in Figure 3.2 is formed for reflectance spectroscopy: a white LED to illuminate the skin, a light transmission probe to deliver the incident light and to collect the reflected light, and a micro spectrometer to evaluate the reflected light. The detailed explanation of the development procedure of this prototype device is given in Chapter 3.

The electronic block diagram of the prototype device is shown in Figure 4.1. The processes are implemented on a 32-bit microprocessor unit and the measured spectra are stored in a flash memory of the prototype device in order to be used in the fitting procedure. The stored results are transferred to a personal computer via USB 2.0 connection. User interface is presented to the users on a 2.8 inches LCD display. The measurement results are shown on the screen. The analog data that is collected by the spectrometer is converted into digital data by a 14 bit ADC. The battery used in the device has a nominal voltage of 3.7 V and a capacity of 1100 mAh enabling at least 1000 cycles of measurements. The light source is driven by a LED driver to supply constant current. The power distribution is achieved by a power regulator that generates 3.3 V for the microprocessor and 5 V for the spectrometer. The device is turned on/off by a switch button.

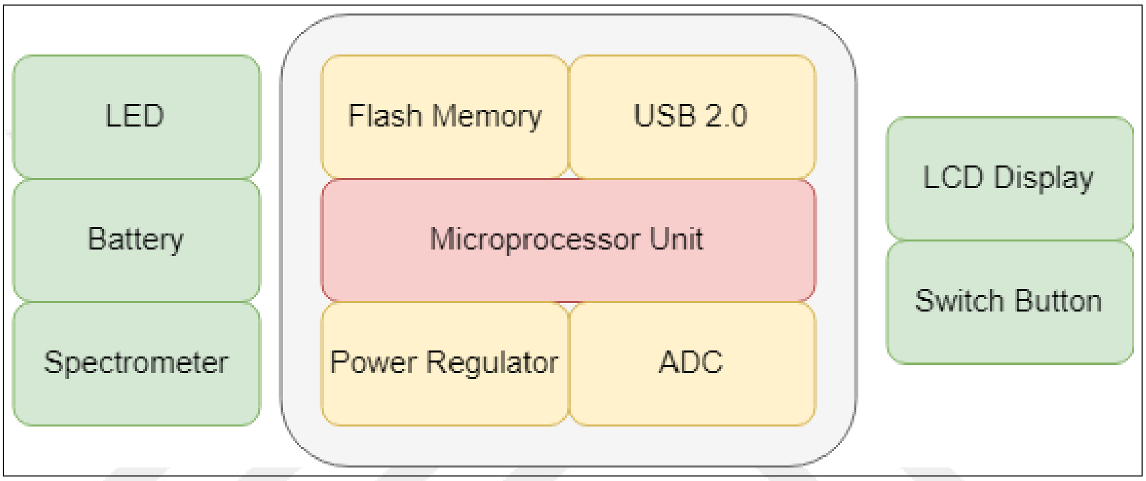

Figure 4.1 The electronic block diagram of the prototype device.

4.2.2 Data Collection

In this study, we used both a prototype device and Draeger JM-103 throughout the whole data collection procedure. Nagar et al. compared TcB measurement devices in terms of TSB determination accuracy [129]. Their test study revealed that JM-103 exhibited a better correlation than the other commonly used device, BiliChek, for TSB measurement. Therefore, in this study JM-103 was chosen as the reference device operating at 450-550 nm wavelength range. Their study also revealed that measurements taken from the sternum have better correlation with the TSB values than the measurements taken from the forehead. In this study, although we took TcB measurements from both the sternum and the forehead, the sternum test data are presented due to its better accepted accuracy.

Blood samples for TSB measurements were taken from a patient group of 314 newborns at the neonatal intensive care unit of Kartal Lutfi Kirdar Hospital in Istanbul. Gestational age and postnatal age of the neonates varied from 32 weeks to 42 weeks and from 12 hours to 144 hours, respectively. Patients who received phototherapy were excluded from the study. The skin type was mostly Type-III, Caucasian. Medical ethical committee approval and consents from the patients' legally authorized representatives were obtained. It was noted that the measurement results were between 0 mg/dl and 25 mg/dl. Hemoglobin breaks down constantly so that bilirubin and hemoglobin concentrations may change over time. If the time between TSB procedure and TcB measurements is long, the bilirubin concentration may change over time and the TcB measurements may not reflect the same TSB level. Although the bilirubin concentration change is slow, in the order of several tens of minutes, we paid special attention to take the TcB measurements immediately after the TSB measurements for the purpose of accurate comparison. During our data collection procedure, TcB measurements were completed within 2 minutes after the TSB procedures. After sampling the blood for TSB analysis, two TcB values were measured and recorded, one with JM-103 and one with the prototype device. Each TcB measurement was completed within a fraction of a second. The entire data collection procedure took 7 months.

TcB measurement results, gestational age in weeks, postnatal age in hours, site of measurement (forehead or sternum), and phototherapy history were recorded by the hospital staff. To minimize reflections from the probe-tissue interface, the probe was touched to the skin surface perpendicularly. Care was taken to keep a constant probe pressure on the patient's skin during each measurement. It is expected that the probe pressure would sensibly affect the transcutaneous measurements of the reflected spectra. To standardize the probe pressure level applied across different measurements, a limit switch is assembled into the prototype device so that the same probe pressure is applied for all measurements. Data recording starts as soon as the switch is turned on. The integration time was 100 ms for each measurement. All TcB measurements were performed by the same pediatric nurse who is well educated and skilled in TcB measurements. The measured reflected spectra were recorded in the memory of the prototype device in order to be used in designing a bilirubin level determination algorithm.

4.2.3 Monte Carlo Simulation of Light Propagation in Neonatal Skin

A general literature overview about Monte Carlo simulations is given in Chapter 3. Here, in this section, in order to better understand the propagation of light in neonatal skin, we made some simulations with the known optical properties of neonates.

In previous research studies, optical properties of the neonatal skin such as absorption coefficient and reduced scattering coefficient were determined as a function of gestational maturity [59]. With these known coefficients, it is possible to make a numerical simulation of the reflectance spectroscopy on neonates' skin with desired concentrations of hemoglobin, melanin and bilirubin.

Lihong Wang and Steven L. Jacques developed Monte Carlo for Multi-Layered media (MCML) to simulate light propagation in neonatal skin affected with different grades of hyperbilirubinemia. They simulate the diffuse reflectance of neonatal skin in the spectral region 400-700 nm [8]. Neonatal skin is modelled as a three-layer structure: epidermis, dermis, and subcutaneous tissue. The Monte Carlo MCML program models the photon transport in multi-layered media, where the optical properties (μ_a, μ_s, g, n) and thickness (d) of each layer are known parameters [130]. Reflectance, transmittance, absorption and fluence can be simulated by this model. Reflectance spectra for different values of bilirubin concentration (C_{bili}, mg/dl), volume fraction of epidermal melanin (f_{me}, %), and volume fraction of blood (f_{bl}, %) of the infants' skin can be obtained as seen in Figure 4.2 and 4.3. These simulations are done in order to determine the three chromophores' effects on reflectance spectra. Each simulation is done using 1 million photons at every wavelength from 400 to 700 nm at 10 nm intervals.

It is observed in Figure 4.2.a that as the concentration of melanin increases, its absorption coefficient increases through the whole VIS spectrum. In Figure 4.2.b, it can be seen that hemoglobin absorption is dominant in the ranges of 400 to 500 nm and

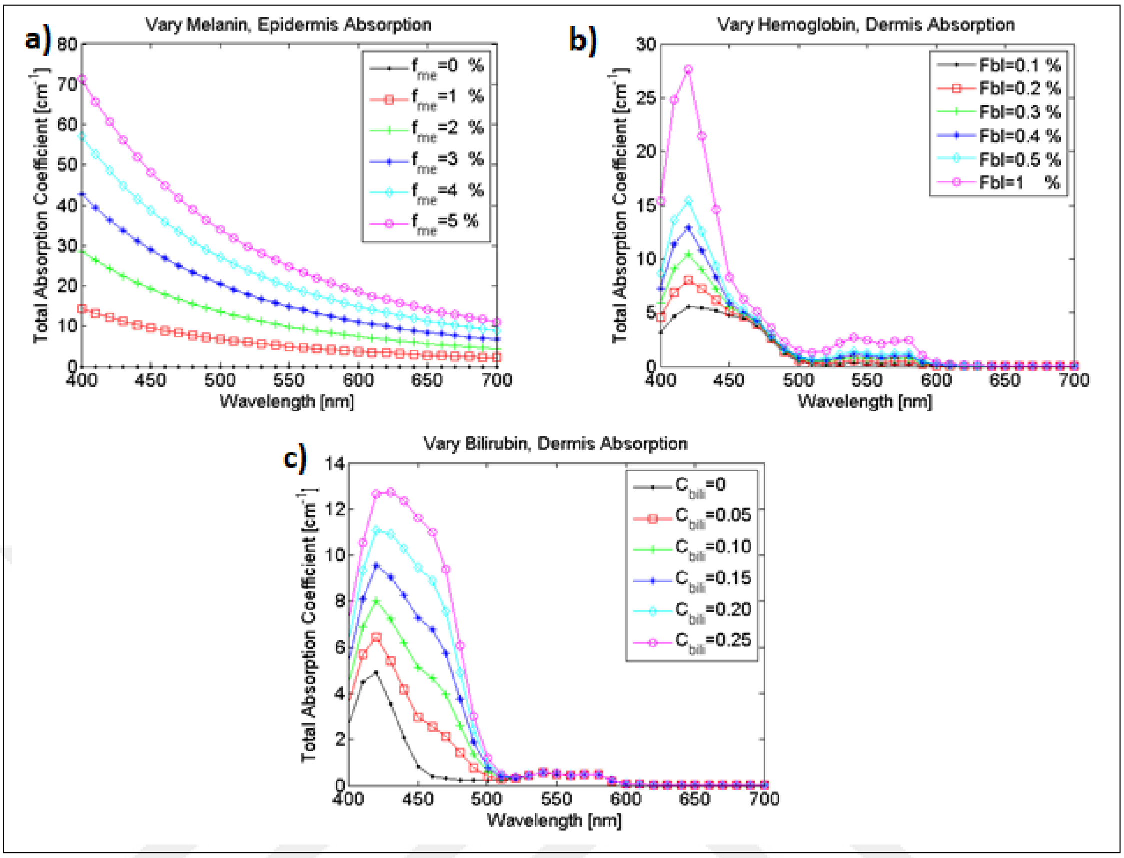

Figure 4.2 a) Diffuse reflectance with varying f_{me}, b) Diffuse reflectance with varying f_{bl}, c) Diffuse reflectance with varying C_{bili}.

500 to 600 nm wavelength and it increases with the hemoglobin concentration. In the last figure, Figure 4.2.c, one can observe that bilirubin absorption is dominant in the wavelength range of 400 to 500 nm and it increases with the bilirubin concentration.

In Figure 4.3 the reflectance spectra of melanin, hemoglobin and bilirubin are shown.

Melanin has a wide absorption spectrum ranging from ultraviolet to near infrared. Its absorption is inversely dependent on the wavelength (λ) as $\lambda^{-3.46}$ [50]. As seen in Figure 4.3.a, a considerable change in the diffuse reflectance of melanin occurs across the entire spectral range.

In the hemoglobin spectrum illustrated in Figure 4.3.b, the impact of blood on the diffuse reflectance R(λ) is maximal in the 540-580 nm region, and there are two local minima and one local maximum in this region. Hemoglobin reflectance decreases as the total hemoglobin concentration increases.

Bilirubin spectrum changes in the range 400-520 nm with respect to the amount of added bilirubin, as depicted in Figure 4.3.c. It is also important to note the nonlinear relationship between bilirubin concentration and diffuse reflectance in the 400-520 nm spectral region.

Considering the reflectance spectra of melanin, hemoglobin and bilirubin, we can now evaluate our own reflectance spectrum obtained from newborn babies in order to calculate the hyperbilirubinemia level.

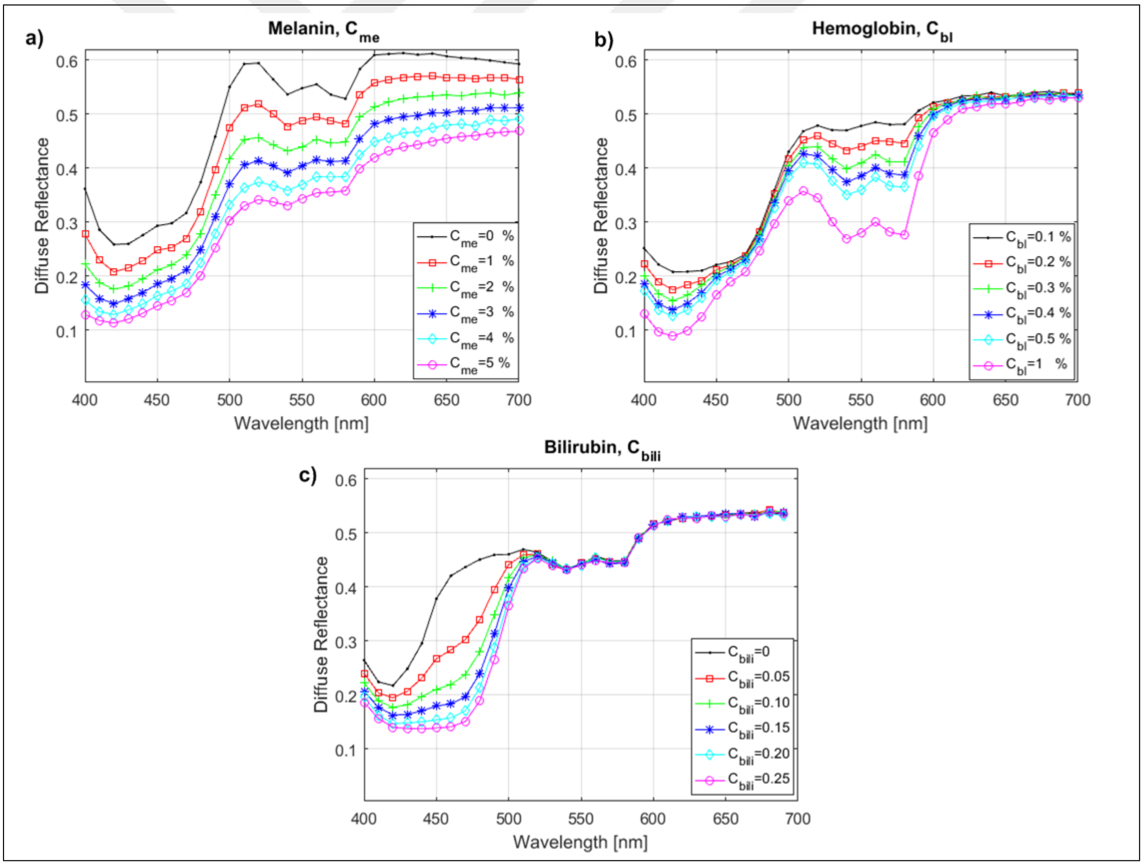

Figure 4.3 a) Diffuse reflectance with varying f_{me}, constant C_{bili}, and constant f_{bl}, b) Diffuse reflectance with varying f_{bl}, constant C_{bili}, and constant f_{me}, c) Diffuse reflectance with varying C_{bili}, constant f_{bl}, and constant f_{me}.

4.2.4 Calibrations

Commercially available JM-103 complies with the related standards and therefore it is already calibrated. For precise and accurate measurements, the prototype device must also be calibrated. We have presented our calibration approach for repeatability purposes. The calibration is achieved in three steps and performed only once. The first step of the calibration is for correcting the frequency offsets of the spectrometer employed as the light sensor of the device shown in Figure 3.2.a. A fluorescent light source with a known power spectrum is used for this purpose. The light emitted by the reference fluorescent source has several peaks at known wavelengths. These peaks as detected by the spectrometer are used to compute the coefficients of a polynomial that characterizes the spectrometer precisely.

Considering that the recorded signal is a factor of light reaching the sensors, suppressing the light results in a recording comprising pure noise and any inherent electronic offset. Therefore, the second step is the removal of dark (noise) current and electronic offset. This is done by first measuring the dark spectrum by recording a measurement in the dark (without lighting the LED) and then subtracting the dark reference (background) spectrum from each of the measured spectra. Removal of the dark reference is described in detail in Section 3.3.

Lastly, the integration time (measurement time) is adjusted to ensure that the power of the light is high enough for achieving a high S/N ratio, but also ensuring that the highest peak in the targeted wavelength range does not cause saturation. Since the same white LED is used for all the measurements and the measured values will be used for training the algorithms of choice, there is no need to identify the incident light intensity as long as the frequency bandwidth is within the VIS.

4.2.5 Melanin and Hemoglobin Effects

The physiology of melanin and interaction of light with it is described in Section 2.2.2. In brief, melanin is a wavelength-dependent attenuation filter absorbing the incident and the reflected light, entering and exiting the tissue [47, 131]. We too observed this behavior in our MCML simulations as depicted in Figure 4.2.a.and Figure 4.3.a. However, melanin light absorption is a nonlinear function of wavelength as it is also the case for hemoglobin and bilirubin. In Figure 4.3, we observe that diffusion reflectance is a function of bilirubin concentration, more pronounced between 400 nm and about 520 nm. While hemoglobin concentration has little influence in the same wavelength range, melanin concentration has a considerable absorption effect on the overall reflectance. Therefore, it is important to eliminate the effect of melanin from the recorded power spectrum, since it is the bilirubin concentration that we seek. Fortunately, there is a band of wavelength in the VIS between 600 nm and 700 nm, where the absorption varies significantly with melanin concentration. Thus, it is possible to eliminate the effect of epidermal melanin with a simple subtraction from the obtained reflected spectrum, leaving bilirubin concentration as the dominant variable [132]. However, in this study, we utilized another method to eliminate the effect of melanin, which is described in [130]. In this method, reflectance values in the recording range of wavelengths are normalized by the maximum reflectance value throughout the whole spectrum, assuming the maximum reflectance is always at the higher wavelengths and dominated by the melanin concentration as in Figure 4.3.

Hemoglobin is another absorber in human skin. Based on the MCML simulation results in Figure 4.3.b, it is seen that hemoglobin has very little effect on the reflectance spectrum where the bilirubin reflectance is dominant. Around 410 nm, hemoglobin effect is quite distinguishable.

4.2.6 Data Analysis

Data analysis was performed using the statistical tools in MATLAB. The correlation between the obtained TcB results and TSB measurements was determined by using Pearson's correlation coefficient (r) given in Eq. 4.1.

$$r = \frac{\sum_{i=1}^{n}(x_i - \overline{x})(y_i - \overline{y})}{\sqrt{\sum_{i=1}^{n}(x_i - \overline{x})^2}\sqrt{\sum_{i=1}^{n}(y_i - \overline{y})^2}} \tag{4.1}$$

where n is the sample size, x_i and y_i are predicted and actual values, $\overline{x}$ and $\overline{y}$ are the mean of predicted and actual values.

The significance of correlation coefficients was assessed by the Student's t-test. A p value less than 0.05 corresponds to a significant correlation, whereas a p value less than 0.001 corresponds to a highly significant correlation. Generally, the linear correlation of two clinical measurements is misleading. Therefore, in order to assess the agreement between TcB and TSB results, Bland-Altman graphs were plotted. The limits of agreement of the mean differences were accepted as 95% confidence intervals (CIs). Also, Shapiro-Wilk Test [133] was used to confirm that the data in the Bland-Altman plots are normally distributed.

A positive bias between the paired values of TSB and TcB (TSB−TcB) indicates that the TcB value is less than the corresponding TSB level and a negative bias is indicative of the TcB measurement being greater than the paired TSB level. The mean absolute error (MAE) calculates the mean of absolute error of TcB values with reference to the corresponding TSB values, see Eq. 4.2

$$MAE = \frac{1}{n}\sum_{t=1}^{n}|y_i - \hat{y}_i| \tag{4.2}$$

where n is the sample size, y_i and $\hat{y}_i$ are the actual and predicted values, respectively.

4.3 Fitting procedure

In the following subsections, applications of the aforementioned nonlinear methods, MPR, ANN and SVR, are described in detail. Selection of input parameters, training process, mathematical approaches, and method-specific parameters are explained in relation to the proposed methods.

4.3.1 Multiple Polynomial Regression Method

In this approach, the measured reflectance values of each spectrum were used as independent variables and the bilirubin level was used as the dependent variable. It is possible to formulate the bilirubin level as in Eq.4.3 assuming it is linearly dependent on the reflected spectrum.

$$B_{level} = \beta_0 + \beta_1 c_1 + \beta_2 c_2 ... + \beta_n c_n + \epsilon \tag{4.3}$$

Here, it is known that c_1, c_2, ... c_n must be correlated with B_{level} but not with each other in order to prevent overfitting and multicollinearity. Therefore, choosing the input parameters in this method is vital and challenging. One should keep in mind that polynomial regression is a form of nonlinear regression that models the relationship between two parameters with an n^{th} degree polynomial. In this study, the response variable (bilirubin level) is nonlinear, i.e., the scatter plot has a nonlinear or curvilinear structure. A general polynomial equation can be defined as in Eq.4.4.

$$y = \beta_0 + \beta_1 x + \beta_2 x^2 ... + \beta_n x^n + \epsilon \tag{4.4}$$

In a similar situation, with one dependent and more than one independent variables, multiple polynomial fitting can be used [134]. A quadratic (second order) polynomial model can be given as in Eq. 4.5

$$y = \beta_0 + \beta_1 x_1 + \beta_2 x_2 + \beta_{11} x_1^2 + \beta_{22} x_2^2 + \beta_{12} x_1 x_2 + \epsilon \qquad (4.5)$$

Polynomial equations become much more complicated if the number of exponential terms increases. Fortunately, a second order polynomial regression is enough in most engineering and manufacturing applications including spectroscopic measurements [135].

It is well known from the literature [59, 8] and shown by the simulation results in Section 4.2.3 that bilirubin absorption coefficient reaches peak level around 465 nm. Therefore, the highest fitting performance between the reflectance values and the bilirubin level would be achieved at that point. Reflectance values at 410 nm are chosen as input parameters when taking the effect of hemoglobin on the obtained spectrum into account. Thus, these two coefficients are chosen as independent variables during the application of quadratic polynomial fitting. To find the best fit, minimization of the sum of squared errors, Least Square Estimation, is used as defined in Eq. 4.6.

$$min \sum_{i=1}^{m} (B_{level_i} - \overline{B_{level}})^2 = min \sum_{i=1}^{m} (B_{level_i} - (\beta X + \epsilon))^2 \qquad (4.6)$$

MPR can be expressed in matrix form in terms of a design matrix $\mathbf{X}$, a response vector B_{level}, a parameter vector $\boldsymbol{\beta}$, and an error vector $\boldsymbol{\epsilon}$.

$$\mathbf{B_{level}} = \boldsymbol{\beta}\mathbf{X} + \boldsymbol{\epsilon} \qquad (4.7)$$

The vector of estimated polynomial regression coefficients can be computed by solving Eq. 4.8 and 4.9 by assuming $\boldsymbol{\epsilon}$ is very close to zero and knowing that $\boldsymbol{X}$ is the non-square matrix.

$$\mathbf{B_{level}X'} = \boldsymbol{\beta}\mathbf{XX'} \qquad (4.8)$$

$$\boldsymbol{\beta} = (\mathbf{X'X})^{-1}\mathbf{X'B}_{\mathbf{level}} \tag{4.9}$$

In order to calculate $\boldsymbol{\beta}$ vector, 70% of the measured spectrum and results chosen by cross validation were used as inputs to the fitting procedure. After finding the fitting coefficients $\boldsymbol{\beta_0}$, $\boldsymbol{\beta_1}$, $\boldsymbol{\beta_2}$, $\boldsymbol{\beta_{11}}$, $\boldsymbol{\beta_{22}}$, and $\boldsymbol{\beta_{12}}$, we tested the fitting equation with the remaining measurements to predict the bilirubin level.

4.3.2 Artificial Neural Network Regression

In this work, we apply ANN as a deep learning tool to predict the bilirubin level using the reflectance measurements at different wavelengths. Note that the relation between the bilirubin concentration and the reflectance measurements is nonlinear. Therefore, a multi-layered neural network structure can be used to model this relation. In this study, we use an ANN architecture consisting of three layers as depicted in Figure 4.4: input layer that accepts reflectance values as input neurons, hidden layer, and one neuron output layer. We performed the experiments by changing the hidden layer number from 2 to 20 by unit step increment. The most accurate bilirubin level prediction is achieved when the hidden layer number is 10. Therefore, we took 10 as the hidden layer number of the ANN.

Design of the ANN architecture and parameter selection were done according to the following considerations:

Network type: Since our network does not contain signal transfer from output to input, we are using a feed-forward network. This is the most popular network architecture in use today [136]. Also, to modify the weight values iteratively, feed-forward backpropagation network would be used.

Input data: Reflectance values in VIS are used as input parameters. There

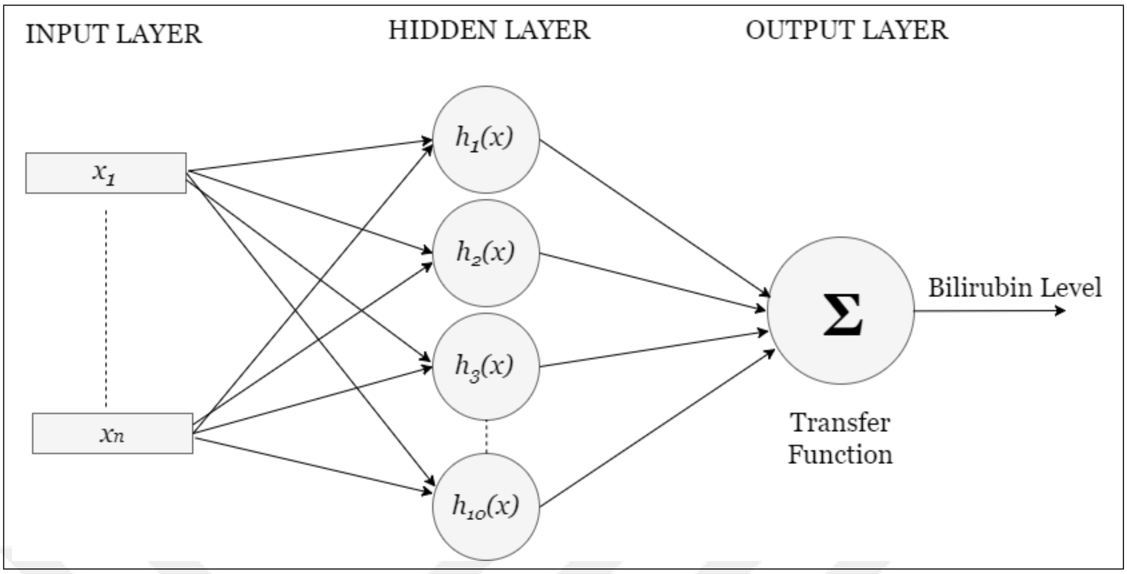

Figure 4.4 ANN architecture for bilirubin level determination.

are 256 input values for each test data.

Target data: Actual TSB measurement results are used as target data.

Number of Layers: The number of hidden layers is chosen as 10 by trial and error.

Layer Properties: As there exists a nonlinear relationship between TcB and TSB measurements, using a smooth, nonlinear activation function is essential for the application of a multi-layer network employing gradient-descent learning. Here, sigmoid function, which is commonly used in backpropagation networks, is used. The last layer (output layer) consists of one neuron with linear (purelin) transfer function. Purelin function is typically used for function approximation or regression tasks [137, 138].

Transfer Functions: The most commonly used transfer functions in neural networks are sigmoid transfer function for hidden layers and purelin transfer function for output layers [139]. The output layer nodes will have bounded output, considering the facts that we are using sigmoid function in the hidden layers, the number of hidden layer nodes is finite, and the gain of the output layer nodes is bounded. Hence, we do not need a sigmoid or tansig function in the output layer.

After training the network with 70% of the test measurements, we performed the simulation with the remaining test measurements, which are determined by cross validation.

4.3.3 Support Vector Regression

While applying the SVR method, the measured reflectance spectra are used as input variables, whereas jaundice levels are taken as observations. The general form of the SVR supposes the existence of a given data set $\boldsymbol{T = (x_i, y_i), i = 1, 2...n \subset XxR}$ such that X represents the space of the independent variables and n denotes the number of the dependent variables. The goal of SVR is to find a function $\boldsymbol{f(x)}$ that has the maximum deviation $\boldsymbol{\epsilon}$ from all targets $\boldsymbol{y_i}$ for all the training data, and at the same time is as flat as possible.

$$\boldsymbol{f(x) = \sum_{i=1}^{n} w_i K(x, x_i) + b} \tag{4.10}$$

where $\boldsymbol{w_i}$ and $\boldsymbol{b}$ represent the weights of the $\boldsymbol{i^{th}}$ feature and the bias, respectively. $\boldsymbol{K(*)}$ is the kernel function and $\boldsymbol{x_i}$ is the $\boldsymbol{i^{th}}$ response. $\boldsymbol{f(x)}$ has the biggest deviation $\boldsymbol{\epsilon}$ from the actual target for all training data.

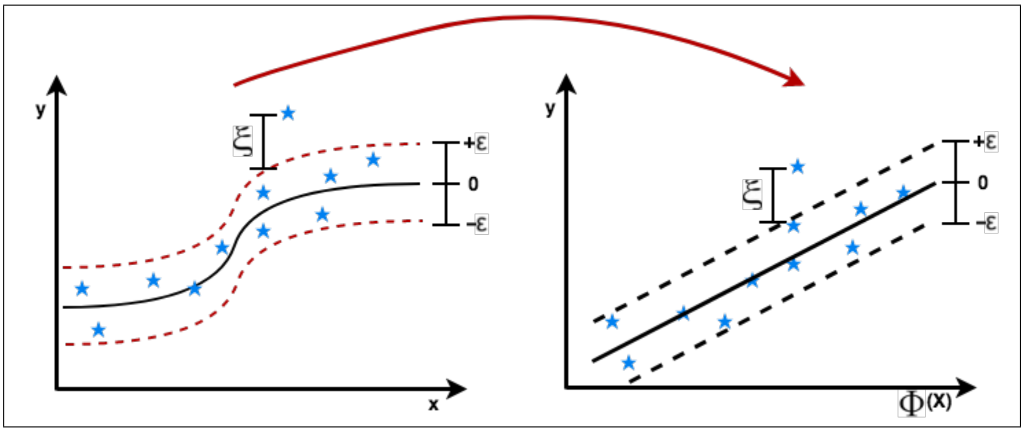

Figure 4.5 Illustration of support vector regression (SVR) to generalize the optimal separating hyperplane in nonlinear separable data.

The flatness of the function $f(x)$ is equivalent to finding the minimum weight vector w. A simple way to derive the required flatness is to minimize the norm: $w^2 = \langle w, w \rangle$. This solution can be formulated as:

$$\text{minimize } \frac{1}{2}\|w\|^2 \\ \text{subject to} \begin{cases} y_i - w^T x_i - b & \leq \epsilon \\ w^T x_i + b - y_i & \leq \epsilon \end{cases} \tag{4.11}$$

However, this is not always feasible. To measure the prediction error, non-negative slack variables ξ, ξ^* are introduced. Then, the optimization problem becomes as follows:

$$\text{minimize } \frac{1}{2}\|w\|^2 + C\sum_{i=1}^{n}(\xi_i + \xi_i^*) \\ \text{subject to} \begin{cases} y_i - w^T x_i - b & \leq \epsilon + \xi_i \\ w^T x_i + b - y_i & \leq \epsilon + \xi_i^* \\ \xi_i, \xi_i^* & \geq 0 \end{cases} \tag{4.12}$$

where x_i is mapped to the higher dimensional space by the kernel function, ξ, and ξ_i^* are the lower and upper training error, C is the regularization constant that determines the trade-off of error margin between the flatness of $f(x)$ and its accuracy in capturing the training data. The constraints of Eq. 4.12 imply that most of the data x_i are inside the tube ϵ. If x_i are outside the tube, it is aimed to minimize the objective function with an error ξ_i, ξ_i^* as depicted in Figure 4.5.

In this study, based on the obtained reflectance values, SVR finds a function, $f(x)$ that can approximate the output to an actual bilirubin level, with error tolerance of ϵ and minimal complexity. The method to be followed in SVR for the nonlinear case is mapping the data onto a richer feature space where they are linearly separable. The general definition of this approach is: $x \rightarrow \Phi(x)$ and $R^d \rightarrow R^D$. The mapping from $\Phi(x)$ to response is given in Eq. 4.13. The systematic representation is depicted in

Table 4.1
Three common kernels

Kernel Name	**Kernel Function**	**Optimization Param.**
Linear	$K(x_n, x_i) = (x_n, x_i)$	C and γ
RBF	$K(x_n, x_i) = exp(-\gamma \|\|x_n - x_i\|\|^2 + C)$	C and γ
Polynomial	$K(x_n, x_i) = (\gamma(x_n, x_i) + r)^d$	C, γ, r, and d

Explanation, C: cost; γ: gamma; r: coefficient; d: degree.

Figure 4.6.

$$f(x) = w^T \Phi(x) + b \tag{4.13}$$

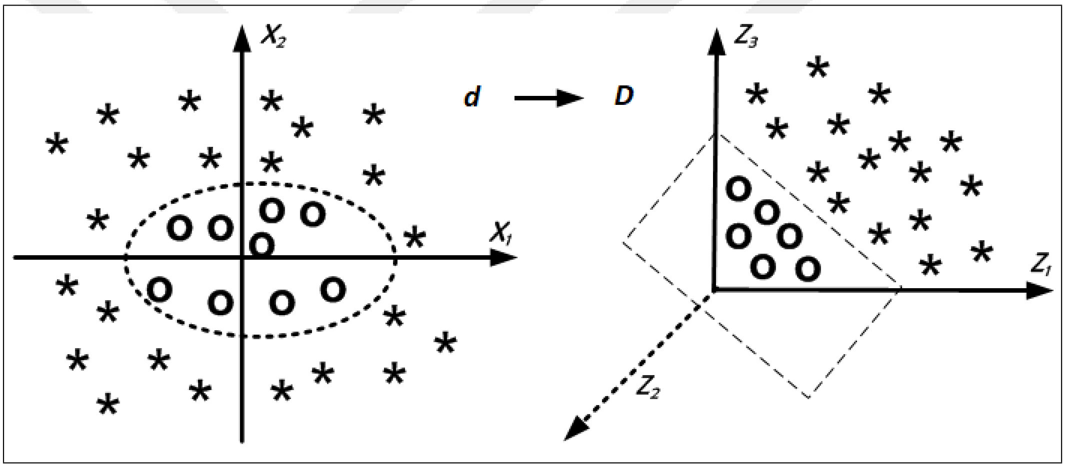

Figure 4.6 Mapping $\Phi(x) : R^2 \rightarrow R^3$

The performance of the function $f(x)$ is affected by the determination of a proper kernel function and ϵ value. There are three types of kernels on SVR models: linear, polynomial, and Gaussian or Radial Basis Function (RBF) tabulated in Table 4.1. A common choice for kernel function is RBF, which generally gives the best results in regression applications. The value of ϵ is influential on the level of accuracy of the approximated function. If ϵ is larger than the target value, it is not possible to obtain good results. If it is zero, overfitting might be an issue.

The reflectance values for wavelengths in VIS are used as input table. There are 256 input values for each measurement. 70% of the measurements were used to find the fitting function and the remaining measurements were used to test the performance.

Many trials were done to get the optimum fitting parameters with different kernels and ϵ values ranging from 0.01 to 2. After each trial, fitting function performance was checked in terms of correlation and error size. Numerous experiments combining training and testing processes were conducted to search for the lowest MAE and the highest r. The best fit was achieved by using linear kernel with the ϵ value of 0.3.

4.4 Results and Analysis

4.4.1 Comparative Analysis

Performance analysis was done by comparing the results of each model, MPR, ANN, and SVR. The mean of the predicted results, r, MAE, p values and biases were calculated. These values were also calculated with the results from Draeger JM-103. The values found via these calculations and those found by the curve fitting applications were compared.

Scatter graphs were plotted in order to depict the correlation between TSB results and the obtained results, and Bland-Altman graphs were plotted to show the error distribution between TSB and the obtained results.

The detailed approaches to parameter selection of MPR, ANN, and SVR methods were described in the relevant sections, 4.3.1, 4.3.2, and 4.3.3. Each patient record comprises one TSB and two TcB data that are taken from the infants' sternum. One of the TcB records is obtained from the commercially available Draeger JM-103 and corresponds to the bilirubin concentration in blood. The second TcB data is obtained from the prototype device yielding 256 reflectance values sampling the VIS spectrum. The patient set was divided into two groups, one (220 samples) for training the algorithms and the other (94 samples) for testing the performance. Cross validation was employed to prevent bias. After finding the calibration curves, they were tested for performance evaluation of prediction. The same test set was used in each method.

4.4.2 Results

TSB values ranged from 1.5 to 22.80 mg/dl, with a mean value of 7.99 ± 4.02 mg/dl. The mean of gestational ages and postnatal ages of the patients were 38.4 ± 1.5 weeks and 2.4 ± 2.5 days, respectively. The distribution of TSB values was as follows: 15% was less than 5 mg/dl, 62% ranged from 5.1 mg/dl to 10 mg/dl, 12% was between 10.1 mg/dl and 15 mg/dl, and 11% was higher than 15 mg/dl. It can be concluded that TSB values are fairly distributed.

The reflectance spectra obtained from infants with different jaundice levels are depicted in Figure 4.7. The raw spectra of the test data are shown in Figure 4.7.a, and the normalized spectra after eliminating the background noise are shown in Figure 4.7.b. In the latter figure, it can be seen that after processing the raw data, the spectra are sorted according to the concentration of bilirubin. By using the reflectance values at 465 nm, it is possible to predict the TSB values with a correlation value of 0.83 in a linear approach.

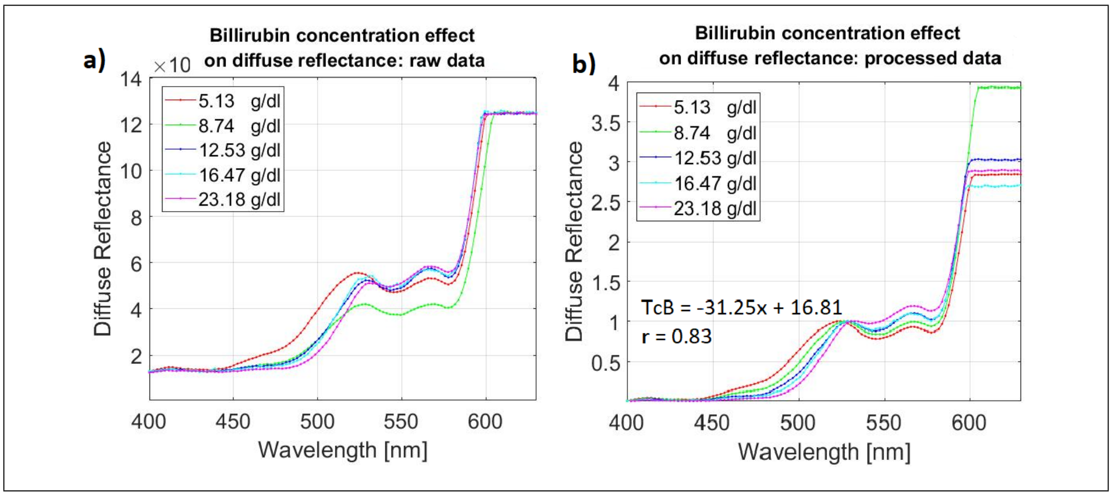

Figure 4.7 Diffuse reflectance spectra obtained from infants with different jaundice levels. a) Effect of bilirubin concentration on diffuse reflectance: raw data, b) Effect of bilirubin concentration on diffuse reflectance: processed data. Linear fitting is achieved with the reflectance values at 465 nm (x values) by using the equation TcB = -31.25*x + 16.81.

In Figure 4.8 the relationship between the TcB and TSB values is depicted.

Highly significant correlations were found in all of the three methods and Draeger JM-103 results. The calculated $\boldsymbol{r}$ values for the total predicted 94 points were 0.938, 0.943, 0.932, and 0.919 ($\boldsymbol{p} < 0.001$) for MPR, ANN, SVR, and Draeger JM-103, respectively.

We calculated the MAE values as 1.03 mg/dl, 1.09 mg/dl, 1.03 mg/dl, 1.35 mg/dl and the means of the predicted TcB values as 8.15±3.51, 8.39±3.50, 8.01±3.33 mg/dl, 7.12±3.75 mg/dl for MPR, ANN, SVR, and Draeger JM-103, respectively.

Figure 4.9 shows the Bland-Altman plots for all comparisons of TcB and TSB. The biases and the 95% CIs are demarcated to determine whether the mean difference between TcB and TSB results are stable at all measured ranges of bilirubin. In all of the applied methods and Draeger JM-103 results, there were very few data values that were outside 2 standard deviations, which suggests normal distribution of data. The biases in predicting TSB values in the application of MPR, ANN, and SVR were -0.17 mg/dl, -0.40 mg/dl, and -0.11 mg/dl with 95% CIs in a range of (-2.93, +2.59) mg/dl, (-3.09, 2.29) mg/dl, and (-3.08, 2.86) mg/dl, respectively, whereas the bias of Draeger JM-103 results was 0.86 mg/dl with a 95% CI in a range of (-3.24, +3.96) mg/dl. The calculated standard deviations of the paired differences were 1.41 mg/dl, 1.37 mg/dl, 1.51 mg/dl, and 1.58 mg /dl, respectively.

In the literature, it is well known that TcB underestimates the TSB levels, especially in higher concentrations (>12 mg/dl)[140]. Therefore, TSB levels greater than 12 mg/dl are of special interest. In our test data, 18 TSB data points are left out of 94 points when a cutoff point of 12 mg/dl is used. The regression analysis between the 18 TSB and the corresponding Draeger JM-103 data results yields $\boldsymbol{r}$ value of 0.615 ($\boldsymbol{p} < 0.05$). On the other hand, $\boldsymbol{r}$ values of MPR, ANN, and SVR with respect to the same TSB results were 0.623, 0.689, and 0.586 ($\boldsymbol{p} < 0.05$), respectively. These correlation values and calculated mean, MAE, bias, and standard deviation of the paired differences are listed in Table 4.2, where each row represents a different measurement type. Note that results of all measurements and results of those higher than 12 mg/dl are shown in sub-rows.

Table 4.2
Statistical results of TcB and TSB measurements

Comparison	Range of Data	N	Mean±SD	r value	MAE	Bias	SD of Diff.
TSB vs TcB-MPR	All TSB	94	8.15±3.51	0.938*	1.03	-0.17	1.41
	TSB >12	18	14.27±2.25	0.623**	1.90	0.96	2.12
TSB vs TcB-ANN	All TSB	94	8.39±3.50	0.943*	1.09	-0.40	1.37
	TSB >12	18	14.41±1.87	0.689**	1.67	0.82	1.87
TSB vs TcB-SVR	All TSB	94	8.01±3.33	0.932*	1.03	-0.11	1.51
	TSB >12	18	13.84±1.60	0.586**	1.76	1.39	2.10
TSB vs TcB-Draeger	All TSB	94	7.12±3.75	0.919*	1.35	0.86	1.58
	TSB >12	18	13.30±1.69	0.615**	2.12	1.93	2.04

TSB values ranged from 1.5 to 22.80 mg/dl with a mean value of 7.99±4.02 mg/dl for all 94 test data points. The mean of 18 TSB test data points higher than 12 mg/dl is 15.23±2.58 . **Range of Data**: Range of the TSB test data, **N**: Number of samples, **Mean±SD**: Mean of TcB values ± Standard Deviation (mg/dl), **r value**: Pearson's Correlation value between TcB and TSB results, *; $p<0.001$ (Highly significant), **; $p<0.05$ (Significant) **MAE**: Mean absolute error between TcB and TSB results (mg/dl), **Bias**: Bias between TSB and TcB results (TSB - TcB) (mg/dl), **SD of Diff.**: Standard Deviation of the paired differences (mg/dl).

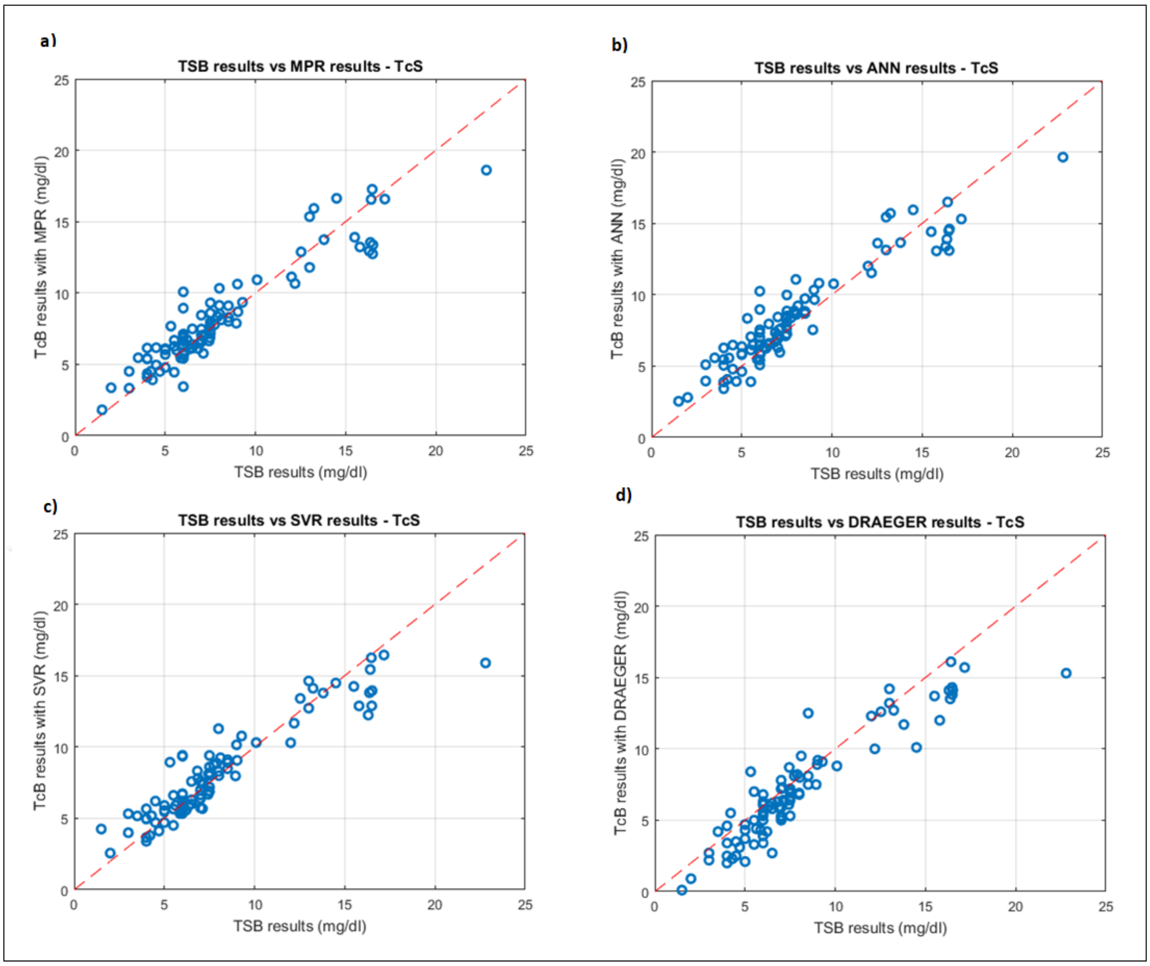

Figure 4.8 TSB results versus TcB results from 94 patients. a) TSB results versus MPR results, b) TSB results versus SVR results, c) TSB results versus ANN results, d) TSB results versus Draeger JM-103 results.

4.5 Discussion

Hyperbilirubinemia is the most common clinical finding that needs to be evaluated and treated in newborns [141]. TSB is the gold standard for detecting and determining newborn Hyperbilirubinemia. TSB is applied by blood sampling with a heel stick. In some newborns, serial TSB measurements are taken to determine not only the bilirubin concentration level but also the rate of change. As the number of TSB measurements increases, it becomes more traumatic and stressful for both parents and patients. Alternatively, transcutaneous bilirubinometry is a useful method that does not need blood sampling for the estimation of neonatal hyperbilirubinemia.

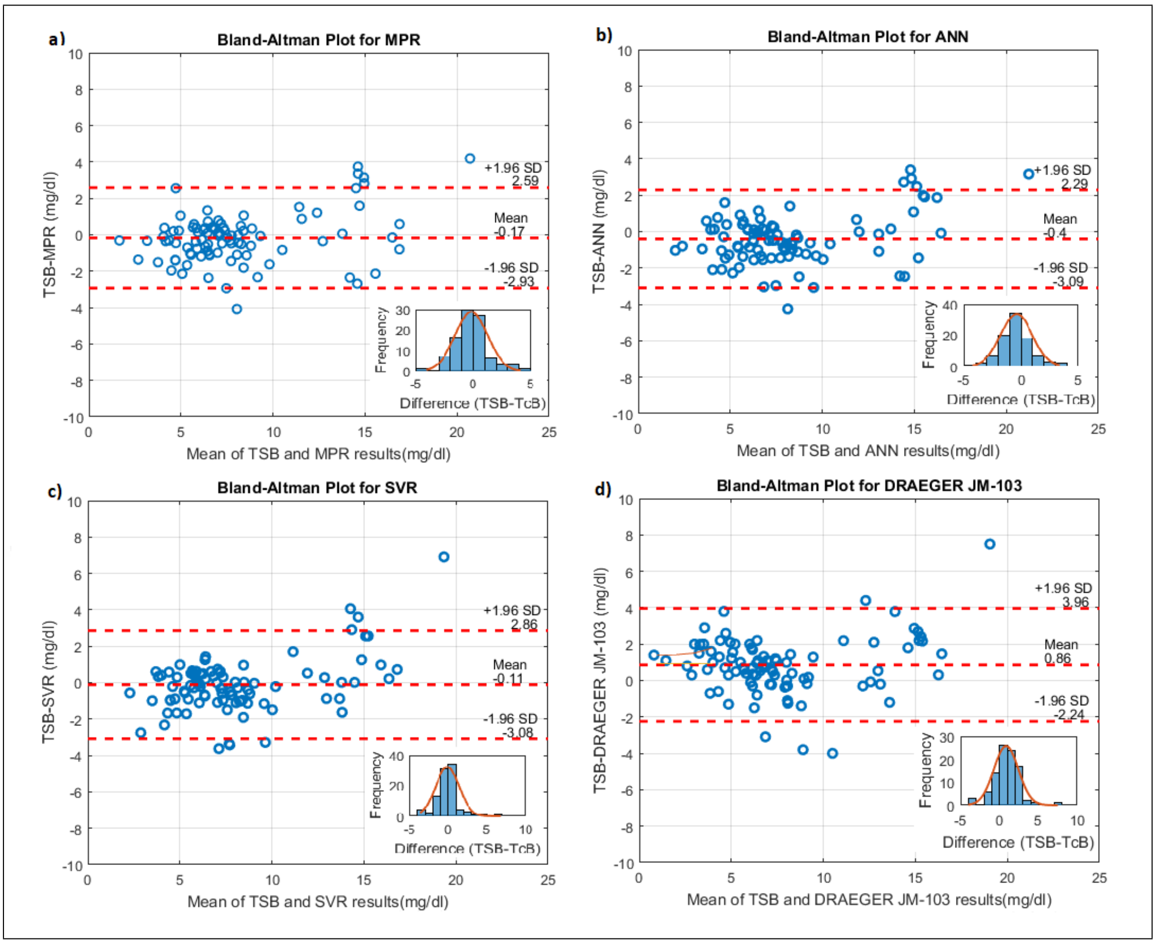

Figure 4.9 Error distribution plot of TSB and TcB for 94 patients. Mean difference between TSB and TcB plotted against mean of TSB and TcB. a) TSB results versus MPR results, b) TSB results versus ANN results, c) TSB results versus SVR results, d) TSB results versus Draeger JM-103 results.

Previous studies indicate that commercial transcutaneous devices correlate well with TSB [142, 143, 144]. The high and significant correlation between TSB and Draeger JM-103 readings (0.919, $p < 0.001$) that we found in our study is in agreement with the studies conducted earlier by using Draeger JM-103 [145, 146].

The main contribution of the current study is the application of three fitting algorithms to predict the jaundice level using real patient data. To the best of our knowledge, ANN and SVR methods are applied for the first time to predict the jaundice level using real patient data. We used a prototype device to collect raw reflectance spectra from the patients. After the data collection part, three algorithms were run offline using a MATLAB program. As a future work, we are planning to perform online prediction using an in-house developed device as well as providing a larger-scale clinical study.

The results of our study indicate that all three nonlinear fitting algorithms, MPR, ANN, and SVR, provide robust estimates of TSB values. Performance evaluation of all range of data (1.5 to 22.80 mg/dl TSB data) shows that while the Draeger JM-103 has a correlation value of 0.919, our three methods predict TSB values with a correlation value in a range of 0.932 to 0.943. In the obtained results, there are marginal differences of 0.02-0.03 in the correlation coefficients and 0.26-0.32 in the errors between Draeger JM-103 and our methods. These results show that the performance of the applied methods is comparable to existing devices. Although this does not lead directly to an increase in the clinical value of transcutaneous bilirubinometry, all three algorithms improve the accuracy of the measurements while ANN yields results closest to the gold standard, TSB.

Another finding of our study is that, although the correlation is quite high for TSB values below 12 mg/dl for all TcB values, the correlation decreases dramatically as the TSB values get higher, as seen in Figure 4.8. This phenomenon has also been discussed in literature [1]. Fortunately, the ANN results for TSB values above 12 mg/dl have noticeably higher $\boldsymbol{r}$, lower MAE and bias values than the Draeger JM-103. This is a significant contribution of our study even though the number of samples above 12 mg/dl is nearly 19% of the total measurements and more measurement samples are required in order to obtain more concrete results.

A further outcome of our study is related to the bias between paired TSB and TcB values. While MPR, ANN, and SVR have a negative bias, Draeger JM-103 has a positive bias for all range of data. The absolute values of the biases for the three applied methods are all lower than the absolute value of bias for the Draeger JM-103 results. All the calculated biases and standard deviations of the paired differences are clinically acceptable and comparable with the results of previous studies that were done with TSB values ranging from 0.0 to 25 mg/dl, where the biases ranged from -1.31 to 1.64 mg/dl and the standard deviation of the paired differences ranged from 0.25 to 2.05 mg/dl [129]. As depicted by the pattern of the plots in Figure 4.9, bias changes based on the TSB level. For TSB values that are higher than 12 mg/dl, bias and standard deviation of the paired differences increases.

Regarding the algorithm design process, the selection of the input parameters of the MPR algorithm can be said to be a challenging task. Accordingly, in order not to increase the complexity of the fitting function, the number of input parameters is chosen as two for the MPR application. These two parameters are determined by considering the results obtained from MCML simulations and our review of the literature. However, during the design of ANN and SVR, all the reflectance values are used as input variables in constructing the prediction algorithms. Therefore, selection of the input parameters in these two methods is relatively easier.

Our study has some limitations. Firstly, TcB reading may be influenced by the gestational age, postnatal age, birth weight, the measurement site on the body, and the record of phototherapy application [147]. Therefore, the influence of these factors should be included as input variables during the design of the bilirubin level detection algorithms. Secondly, as the jaundice level increases, TcB tends to underestimate bilirubin in comparison to TSB [148]. This is mainly caused by the physiologic difference between TSB and TcB. While TSB measures the intravascular bilirubin, TcB measures the extravasated bilirubin [9]. The relation between these two bilirubin values is not fully specified, especially in patients with high bilirubin levels. Therefore, the correlation between TcB and TSB is decreasing. However, it seems possible to improve this by ANN learning. Unfortunately, there are not enough measurements of high level bilirubin in our study to educate the network.

It is worth mentioning one more issue about the measurement setup. As stated before, bilirubin absorption spectra yield in the range of 420 to 480 nm. With a white LED, it is possible to illuminate the whole VIS, but the power intensity for each wavelength is not equally distributed. As seen in Figure 4.7, the reflectance values in bilirubin reflectance spectra are relatively smaller than those in the range of 480 to 700 nm. In order to increase the S/N ratio for the bilirubin reflectance values, light power is increased on purpose at the cost of causing some saturation in the higher wavelengths of the spectrum. The saturated region is known to be unrelated to bilirubin concentration as seen in Figure 4.3. For our purpose, we have incremented the integration time to such a level that saturation is seen above 600 nm wavelength.

4.6 Conclusion

Neonatal jaundice is a potentially life-threatening disease that requires accurate, noninvasive, easy-to-use, and fast ways to monitor the disease before it can cause permanent damage. Optical techniques provide noninvasive tools to achieve this objective. The current work consists of the development of a prototype device that employs optical techniques, and the design of bilirubin detection algorithms that utilize mathematical methods.

The prototype device was designed to make use of reflectance spectroscopy. By using this prototype device, we carried out a large-scale clinical study to measure reflectance spectra of jaundiced newborns. To analyze the obtained reflectance spectra, bilirubin level detection algorithms were designed via three mathematical methods, namely MPR, ANN, and SVR. Then, their performance was tested against invasive but well accepted TSB measurements. All three methods achieved acceptable precision and accuracy in predicting the jaundice level in terms of $\boldsymbol{r}$, MAE, and bias values. The highest $\boldsymbol{r}$ value was calculated in the ANN method while the lowest MAE value was equal in the MPR and SVR methods. All three applied methods had a negative bias value, which indicates that all methods provided higher results on the average compared to TSB. The smallest absolute bias value was found when the SVR method was applied. It is observed that the ANN method provides slightly better results than the other methods in terms of correlation with TSB.

Also, it can be concluded that by applying the MPR, ANN, and SVR methods, we can get slightly better results than commercial products. Especially, in the application of ANN, better correlation results are obtained at higher jaundice levels for which clinical laboratory confirmation is recommended.

Our immediate future plan is improving our algorithms with a much larger data set at higher jaundice levels. With this study, we realized that there is an enormous scope for improvement of transcutaneous bilirubinometers by using nonlinear fitting algorithms. These outcomes are encouraging towards increasing the clinical use of transcutaneous bilirubinometers.

5. GENERAL SUMMARY AND FUTURE DIRECTIONS

5.1 Overview

The overall objective of this dissertation was to determine newborn jaundice level with improved accuracy of noninvasive bilirubinometers. For this purpose, we designed nonlinear regression methods to predict the bilirubin concentration in blood. In order to collect data from the jaundiced babies to be used in the algorithm design process, we built an in-house prototype transcutaneous bilirubinometer.

The prototype device was developed to make use of reflectance spectroscopy. The main components of this device were a light source to illuminate the skin surface, a light transmission probe to transmit the generated and reflected light, and a detector to evaluate the collected light.

With the help of this prototype device, we carried out a large-scale clinical study in a neonatal clinic and collected reflectance spectra of the jaundiced newborns. All the measured spectra were recorded with their paired TSB values. We designed three prediction algorithms to determine the jaundice level by making use of these recorded data.

The designed fitting algorithms were compared by evaluating their predictive performance in determining the jaundice level in newborns. We also compared the predicted results with the measured results of Draeger JM-103, which is a commonly used commercially available transcutaneous bilirubin measurement device. The results were promising towards increasing the clinical value of transcutaneous bilirubinometers.

5.2 Implications

This thesis describes a simple and applicable method to determine newborn jaundice in a noninvasive manner. A simple optic probe design is described in detail. By following the technical details in this dissertation, one can design their own optic probe to be used in a DRS measurement system.

Additionally, during this thesis study we designed nonlinear methods providing improved precision in transcutaneous bilirubinometry. Implementation of these methods are described elaborately through the dissertation by explaining the selection of input parameters, training process, mathematical approaches, and method-specific parameters. Thus, it is possible to use these algorithms in any DRS measurement application.

Another implication of this study is that we obtained more precise results than Draeger JM-103. This shows that using nonlinear methods can provide improvements in the transcutaneous bilirubinometry.

The prices of Philips BiliChek and Draeger JM-103, which are the most commonly used devices in the market, vary between \$6K and \$9K. This price range is relatively high and limits the use of these devices. The designed prototype device in this thesis costs less than \$1K which makes it more affordable. We think that a handheld, easy to produce, more precise, and commercially competitive transcutaneous bilirubinometer can be manufactured.

Since the developed DRS system works in the whole VIS range, it can be used not only for jaundice determination but also for other diagnostic applications from the skin surface such as hemoglobin level determination, skin cancer detection, and bruise detection for forensic applications.

5.3 Future Directions

According to a new report published by Gen Consulting Company, global jaundice meter market is expected to grow at a compound annual growth rate (CAGR) of 4.1% by 2022 [149]. The report includes a forecast of the size of the jaundice meter market and an analysis on a global and regional level including North America, Europe, Asia-Pacific, MEA and South America. This research report also states that steady growth till 2023 by top vendors, end users, and by applications will be seen. The current total market size is $75M and the number of jaundice meters sold every year is around 50 thousand. From the results given in the report, it is obvious that there are big opportunities in the jaundice meter device market. Especially, in developing countries, where current transcutaneous bilirubinometers, such as Draeger JM-105, Natus, and Philips BiliChek, are considered to be relatively expensive, presenting a more affordable device will increase the usage of jaundice meters.

Using the technical details of the optical probe described in this thesis and the designed algorithms, a very compact device connected to smart phones can be produced. However, using a spectrometer as a detector in the design increases the cost and the size of the device considerably. According to the results of our first studies, using a RGB color sensor instead of a spectrometer gives sufficiently precise results in DRS measurements. In addition, using a color sensor as a detector will dramatically reduce the production cost to less than $10. This price reduction will enable the selling of such a device in pharmacies, which is unprecedented. Moreover, with the mobile application that can show the results to users, it can be used by everyone without the need for a health personnel. This will provide an important solution for the detection of jaundice, especially in developing countries such as Africa, where transcutaneous bilirubinometer devices are not widely used.

APPENDIX A. LIST OF PUBLICATIONS PRODUCED FROM THE THESIS

1. Yunus Karamavuş, Mehmed Özkan, Newborn jaundice determination by reflectance spectroscopy using multiple polynomial regression, neural network, and support vector regression, Biomedical Signal Processing and Control, Volume 51, 2019, Pages 253-263, ISSN 1746-8094,

   https://doi.org/10.1016/j.bspc.2019.01.019.

2. Y. Karamavuş and M. Özkan, "Determination of newborn jaundice level by transcutaneous bilirubin measurement," 2018 26th Signal Processing and Communications Applications Conference (SIU), Izmir, 2018, pp. 1-4.

   doi: 10.1109/SIU.2018.8404218

3. Y. Karamavuş, H. B. Çelebi, Y. Uludağ and M. Özkan, "Design of a new optic probe for diffuse reflectance spectroscopy," 2015 23nd Signal Processing and Communications Applications Conference (SIU), Malatya, 2015, pp. 2206-2209. doi: 10.1109/SIU.2015.7130313

APPENDIX B. USER INTERFACE OF THE TEST PROGRAM

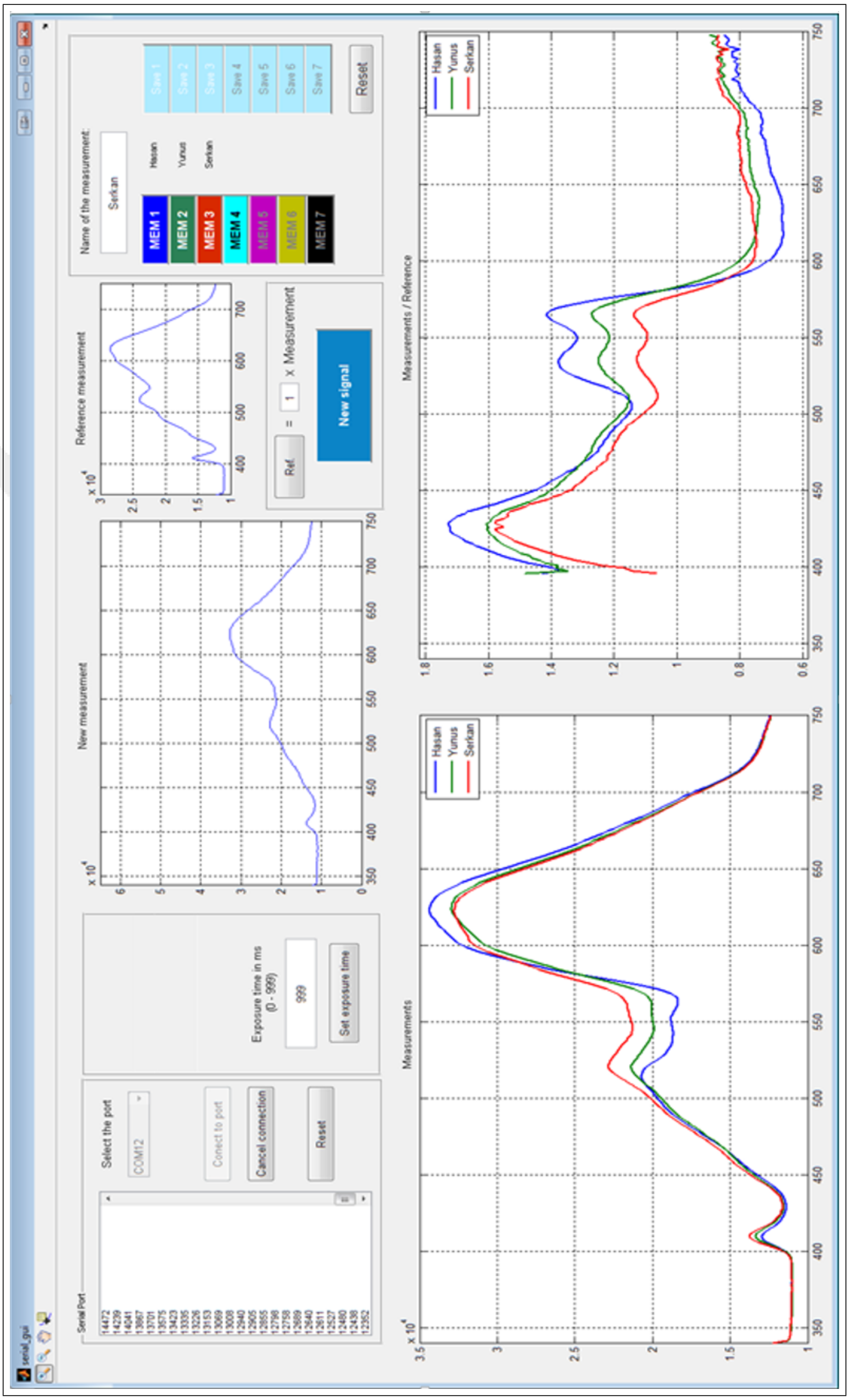

```
14472
14239
14041
13867
13701
13575
13423
13335
13226
13153
13069
13008
12940
12905
12855
12798
12758
12689
12640
12611
12527
12480
12438
12362
```

Exposure time in ms (0 - 999): 999

Name of the measurement: Serkan

Figure B.1 User interface of the test program to investigate the measured reflectance data.

REFERENCES

1. El-Beshbishi, S. N., K. E. Shattuck, A. A. Mohammad et al., “Hyperbilirubinemia and transcutaneous bilirubinometry,” *Clinical Chemistry*, Vol. 55, no. 7, pp. 1280–1287, 2009.

2. Shapiro, S., “Bilirubin toxicity in the developing nervous system,” *Pediatric Neurology*, Vol. 29, pp. 410–21, 12 2003.

3. American Academy of Pediatrics, “Management of hyperbilirubinemia in the newborn infant 35 or more weeks of gestation,” *Pediatrics*, Vol. 114, no. 1, pp. 297–316, 2004.

4. Lilien, L., V. Harris, R. Ramamurthy et al., “Neonatal osteomyelitis of the calcaneus: complication of heel puncture,” *The Journal of Pediatrics*, Vol. 88, p. 478—480, March 1976.

5. Romagnoli, C., E. Zecca, P. Catenazzi et al., “Transcutaneous bilirubin measurement: Comparison of respironics bilicheck and jm-103 in a normal newborn population,” *Clinical Biochemistry*, Vol. 45, pp. 659–62, 03 2012.

6. Grohmann, K., M. Roser, B. Rolinski et al., “Bilirubin measurement for neonates: Comparison of 9 frequently used methods,” *Pediatrics*, Vol. 117, pp. 1174–83, 05 2006.

7. Randeberg, L. L., E. Bruzell, L. Nilsen et al., “In vivo spectroscopy of newborn skin reveals more than a bilirubin index,” *Acta Paediatrica (Oslo, Norway : 1992)*, Vol. 94, pp. 65–71, 02 2005.

8. Wang, L., S. L. Jacques, and L. Zheng, “Mcml—monte carlo modeling of light transport in multi-layered tissues,” *Computer Methods and Programs in Biomedicine*, Vol. 47, no. 2, pp. 131 – 146, 1995.

9. Bosschaart, N., J. H. Kok, A. M. Newsum et al., “Limitations and opportunities of transcutaneous bilirubin measurements,” *Pediatrics*, Vol. 129, no. 4, pp. 689–694, 2012.

10. M Balabin, R., and E. Lomakina-Rumyantseva, “Neural network approach to quantum-chemistry data: Accurate prediction of density functional theory energies,” *The Journal of Chemical Physics*, Vol. 131, p. 074104, 09 2009.

11. Naes, T., T. Isaksson, T. Fearn et al., *A User Friendly Guide to Multivariate Calibration and Classification*, 01 2002.

12. K Bhutani, V., A. Zipursky, H. Blencowe et al., “Neonatal hyperbilirubinemia and rhesus disease of the newborn: incidence and impairment estimates for 2010 at regional and global levels,” *Pediatric Research*, Vol. 74 Suppl 1, pp. 86–100, 12 2013.

13. Burke, B., J. Robbins, T. Mac Bird, C. Hobbs et al., “Trends in hospitalizations for neonatal jaundice and kernicterus in the united states, 1988-2005,” *Pediatrics*, Vol. 123, pp. 524–32, 03 2009.

14. Hamer, D., “Clinical signs that predict severe illness in children under age 2 months: a multicentre study young infants clinical signs study group lancet 2008 371 135 142 10.1016/s0140-6736(08)60106-3 18191685,” *The Lancet*, Vol. 371, 01 2008.

15. Dai, J., D. M. Parry, and J. Krahn, “Transcutaneous bilirubinometry: Its role in the assessment of neonatal jaundice,” *Clinical Biochemistry*, Vol. 30, no. 1, pp. 1 – 9, 1997.

16. Group, S. P., "Newborn jaundice," 2019. Online; accessed January 30, 2019.

17. Nag, N., S. Halder, R. Chaudhuri et al., "Role of bilirubin as antioxidant in neonatal jaundice and effect of ethanolic extract of sweet lime peel on experimentally induced jaundice in rat," *Indian Journal of Biochemistry Biophysics*, Vol. 46 1, pp. 73–8, 2009.

18. Ruth D. Nass, Y. F., ed., *Cognitive and Behavioral Abnormalities of Pediatric Diseases*, 198 Madison Avenue, New York, New York 10016: Oxford University Press, 2010.

19. Boyd, S., "Treatment of physiological and pathological neonatal jaundice," *Nursing Times*, Vol. 100, pp. 40–3, 03 2004.

20. Jana, B., *Gynaecology and Obstetrics*, New Delhi 110055: B. Jain Publisherss, 2005.

21. A. Pearson, H., "Life span of the fetal red blood cell," *The Journal of Pediatrics*, Vol. 70, pp. 166–71, 03 1967.

22. Lauer, B., and N. Spector, "Hyperbilirubinemia in the newborn," *Pediatrics in Review / American Academy of Pediatrics*, Vol. 32, pp. 341–9, 08 2011.

23. De Steuben, C., "Breast-feeding and jaundice. a review," *Journal of Nurse-Midwifery*, Vol. 37, pp. 59S–66S, 03 1992.

24. Melton, K., and H. Akinbi, "Neonatal jaundice strategies to reduce bilirubin-induced complications," *Postgraduate Medicine*, Vol. 106, pp. 167–8, 171, 12 1999.

25. Kotal, P., C. van der Veere, M. Sinaasappel et al., "Intestinal excretion of unconjugated bilirubin in man and rats with inherited unconjugated hyperbilirubinemia," *Pediatric research*, Vol. 42, pp. 195–200, 08 1997.

26. Welsh, A., ed., *National Collaborating Centre for Women's and Children's Health (UK). Neonatal Jaundice, NICE Guideline*, London NW1 4RG: CRC, 2010. Available: https://www.ncbi.nlm.nih.gov/books/NBK65120/.

27. Kazmierczak, S. C., A. F. Robertson, P. G. Catrou et al., "Direct spectrophotometric method for measurement of bilirubin in newborns: Comparison with hplc and an automated diazo method," *Clinical Chemistry*, Vol. 48, no. 7, pp. 1096–1097, 2002.

28. Leica Optical Systems Division, *Leica Unistat bilirubinometer instruction manual*, Buffalo, NY:Leica,: Leica Inc, 1997:23pp.

29. Ip, S., M. Chung, J. Kulig, R. O'Brien et al., "Subcommittee on hyperbilirubinemia. an evidence-based review of important issues concerning neonatal hyperbilirubinemia," *Pediatrics*, Vol. 114, p. e130–e153, 01 2004.

30. Kaplan, M., and C. Hammerman, "Understanding and preventing severe neonatal hyperbilirubinemia: Is bilirubin neurotoxity really a concern in the developed world?," *Clinics in Perinatology*, Vol. 31, pp. 555–75, x, 10 2004.

31. Draeger Inc., "Draeger jaundice meter jm-105." Brochure, 2019.

32. Mennen, "Bilicare-neonatal noninvasive bilirubin meter." Brochure, 2019.

33. Taylor, J., J. Stout, L. de Greef et al., "Use of a smartphone app to assess neonatal jaundice," *Pediatrics*, Vol. 140, p. e20170312, 08 2017.

34. De Greef, L., M. Goel, M. Joon Seo et al., “Bilicam: Using mobile phones to monitor newborn jaundice,” *UbiComp 2014 - Proceedings of the 2014 ACM International Joint Conference on Pervasive and Ubiquitous Computing*, pp. 331–342, 09 2014.

35. Munkholm, S. B., T. Krogholt, F. Ebbesen et al., “The smartphone camera as a potential method for transcutaneous bilirubin measurement,” *PloS One*, 03 2018.

36. Kaufmann Mike LeMaster, P. M., and K. Morrison-Graham, *Anatomy and Physiology*, Open Oregon State, Oregon State University, 2019.

37. Ezzat, W., H. Ghandoor, H. Henawi, and Y. El-Sharkawy, “Discrimination of skin micro-textures using intelligent laser speckle technique,” *International Journal of Advanced Research*, Vol. 6, pp. 210–222, 10 2018.

38. Anderson, R. R., and J. A. Parrish, “The optics of human skin,” *Journal of Investigative Dermatology*, Vol. 77, no. 1, pp. 13 – 19, 1981.

39. Agar, N., and A. Young, “Agar n, young armelanogenesis: a photoprotective response to dna damage? mutat res 571:121-132,” *Mutation Research*, Vol. 571, pp. 121–32, 05 2005.

40. Kim, O., J. McMurdy, C. Lines et al., “Reflectance spectrometry of normal and bruised human skins: Experiments and modeling,” *Physiological Measurement*, Vol. 33, pp. 159–75, 02 2012.

41. Sandby-Moller, J., T. Poulsen, and H. Wulf, “Epidermal thickness at different body sites: Relationship to age, gender, pigmentation, blood content, skin type and smoking habits,” *Acta Dermato-Venereologica*, Vol. 83, pp. 410–3, 02 2003.

42. Tony Burns MB, BS, F. S. B., ed., *Book’s Textbook of Dermatology, Volume 1, 8th Ed.*, Blackwell Publishing Ltd, 2010.

43. Cent, R. M. L., “Optical properties spectra,” 2019. Online; accessed January 30, 2019.

44. Bhandari, A., B. Hamre, O. Frette et al., *Modeling optical properties of human skin using Mie theory for particles with different size distributions and refractive indices*, Opt. Express, 2011.

45. Eames, M., J. Wang, B. W Pogue, and H. Dehghani, “Wavelength band optimization in spectral near-infrared optical tomography improves accuracy while reducing data acquisition and computational burden,” *Journal of Biomedical Optics*, Vol. 13, p. 054037, 09 2008.

46. Suh, EunJung, W. Youngah, and K. HyoJin, “Determination of water content in skin by using a ft near infrared spectrometer,” *Archives of Pharmacal Research*, Vol. 28, pp. 458–62, 05 2005.

47. Van Gemert, M., S. Jacques, H. Sterenborg, and W. M Star, “Skin optics,” *IEEE Transactions on Bio-medical Engineering*, Vol. 36, pp. 1146–54, 01 1990.

48. Fitzpatrick, T. B., “The Validity and Practicality of Sun-Reactive Skin Types I Through VI,” *Archives of Dermatology*, Vol. 124, pp. 869–871, 06 1988.

49. Kollias, N., and A. H. Baqer, “Absorption mechanisms of human melanin in the visible, 400–720 nm,” *The Journal of Investigative Dermatology*, Vol. 89, pp. 384–8, 11 1987.

50. L Wolbarsht, M., A. W Walsh, and G. George, “Melanin, a unique biological absorber,” *Applied Optics*, Vol. 20, pp. 2184–6, 07 1981.

51. Sarkar, R., S. Basu, R. K Agrawal et al. , “Skin care for the newborn,” *Indian Pediatrics*, Vol. 47, pp. 593–8, 07 2010.

52. Tom Lister, Philip A. Wright, and P. H. Chappel, “Optical properties of human skin,” *Journal of Biomedical Optics*, Vol. 17, pp. 17 – 17 – 15, 2012.

53. Randeberg, L. L., *Doctoral Thesis. Diagnostic applications of diffuse reflectance spectroscopy.* PhD thesis, NTNU University, Trondheim,, 2005.

54. Coburn, R., R. E Forster, and P. B Kane, “Consideration of the physiological variables that determine the blood carboxyhemoglobin concentration in man,” *The Journal of Clinical Investigation*, Vol. 44, pp. 1899–910, 12 1965.

55. F McDonagh, A., and D. A Lightner, “’like a shrivelled blood orange’ - bilirubin, jaundice, and phototherapy,” *Pediatrics*, Vol. 75, pp. 443–55, 04 1985.

56. Stevenson, D.K., M. Jeffrey Maisels, J. F. Watchko, *Care of the Jaundiced Neonate 1st Edition*, McGraw-Hill Education, 2012.

57. Virchow, R. V., “Die pathologischen pigmente,” *Archiv für Pathologische Anatomie und Physiologie und Für klinische Medicin*, Vol. 1, pp. 379–404, 2005.

58. Yan, D., C. Domes, R. Domes, T. Frosch et al., “Fiber enhanced raman spectroscopic analysis as a novel method for diagnosis and monitoring of diseases related to hyperbilirubinemia and hyperbiliverdinemia,” *Analyst*, Vol. 141, pp. 6104–6115, 2016.

59. Saidi, I. S., *Transcutaneous optical measurement of hyperbilirubinemia in neonates.* PhD thesis, Rice University, Houston, USA, 1992.

60. Saidi, I. S., S. Jacques, and F. Tittel, “Mie and rayleigh modeling of visible-light scattering in neonatal skin,” *Applied Optics*, Vol. 34, pp. 7410–8, 11 1995.

61. Classroom, T. P., “Reflection and the ray model of light, lesson-1, reflection and its importance,” 2019. Online; accessed February 10, 2019.

62. Yang, Y.L., A. Katz, E. J. Celmer et al., “Optical spectroscopy of benign and malignant breast tissue,” *Lasers Life Sci*, Vol. 7, 04 1996.

63. Bigio, I., S.G. Bown, G. Kelley et al., “Diagnosis of breast cancer using elastic-scattering spectroscopy: preliminary clinical results,” *Journal of Biomed Opt*, Vol. 5:221-8, 04 2000.

64. Wisner, D., A. Cerussi, F. Bevilacqua et al., “Monitoring neoadjuvant chemotherapy in breast cancer using quantitative diffuse optical spectroscopy: A case study,” *Journal of Biomedical Optics*, Vol. 9, pp. 230–8, 01 2004.

65. Zonios, G., L.T. Perelman, V. Backman et al., “Diffuse reflectance spectroscopy of human adenomatous colon polyps in vivo,” *Applied Optics*, Vol. 38, pp. 6628–6637, 1999.

66. Liu, Q., “Role of optical spectroscopy using endogenous contrasts in clinical cancer diagnosis,” *World J Clinical Oncology*, Vol. 2, pp. 50–63, 01 2011.

67. Lariviere, B., K. S. Garman, N. Lynn Ferguson et al., “Spatially resolved diffuse reflectance spectroscopy endoscopic sensing with custom si photodetectors,” *Biomedical Optics Express*, Vol. 9, p. 1164, 03 2018.

68. Ohka, M., Y. Mitsuya, I. Higashioka, and H. Kabeshita, “An experimental optical three-axis tactile sensor for micro machines.,” *Transactions of the Japan Society of Mechanical Engineers Series C*, Vol. 66, 07 2005.

69. Zonios, G. and A. Dimou, “Modeling diffuse reflectance from semi-infinite turbid media: application to the study of skin optical properties,” *Optical Society of America*, 2006.

70. Taroni, P., A. Bassi, D. Comelli et al., “Diffuse optical spectroscopy of breast tissue extended to 1100 nm,” *Journal of Biomedical Optics*, Vol. 14, p. 054030, 09 2009.

71. Hsu, C.K., S.Y. Tzeng, C.C. Yang et al., “Non-invasive evaluation of therapeutic response in keloid scar using diffuse reflectance spectroscopy,” *Biomedical Optics Express*, Vol. 6, 02 2015.

72. Yudovsky, D., and L. Pilon, “Rapid and accurate estimation of blood saturation, melanin content, and epidermis thickness from spectral diffuse reflectance,” *Applied Optics*, Vol. 49, pp. 1707–19, 04 2010.

73. J. Farrell, T., M. S. Patterson, and B. C. Wilson, “A diffusion theory model of spatially resolved, steady-state diffuse reflectance for the noninvasive determination of tissue optical properties in vivo,” *Medical Physics*, Vol. 19, pp. 879–88, 07 1992.

74. Bays, R., Wagnieres, G., Robert, D., Braichotte, D. et al., “Clinical determination of tissue optical properties by endoscopic spatially resolved reflectometry,” *Applied Optics*, Vol. 35, no. 10, pp. 1756–1766, 1996.

75. Metropolis, C., and N.M. Ulam, “The monte carlo method[U+2B1A] [U+2B1A],” *Journal of the American Statistical Association*, Vol. 44, pp. 335–341, 10 1949.

76. J. Welch, A., and M. J. C. van Gemert, *In Optical-Thermal Responses of Laser-Irradiated Tissue 2nd Edition*, Springer, 2009.

77. Wang, L.H., and W. Hsini, *Biomedical Optics: Principles and Imaging*, Wiley, May 2007.

78. Prahl, S., M. Keijzer, S. Jacques, and A. J. Welch, “A monte carlo model of light propagation in tissue,” *SPIE Inst. Ser. IS*, Vol. 5, 01 1989.

79. Karamavuş, Y., H. B. Çelebi, Y. Uludağ, and M. Özkan, “Design of a new optic probe for diffuse reflectance spectroscopy,” in *2015 23nd Signal Processing and Communications Applications Conference (SIU)*, pp. 2206–2209, May 2015.

80. Yu, B., A. Shah, V. K. Nagarajan, and D. G Ferris, “Diffuse reflectance spectroscopy of epithelial tissue with a smart fiber-optic probe,” *Biomedical Optics Express*, Vol. 5, pp. 675–89, 03 2014.

81. Lin, W.C., A. Mahadevan-Jansen, M. D. Johnson et al., “In Vivo Optical Spectroscopy Detects Radiation Damage in Brain Tissue,” *Neurosurgery*, Vol. 57, pp. 518–525, 09 2005.

82. Utzinger, U., and R. Richards-Kortum, “Fiber optic probes for biomedical optical spectroscopy,” *Journal of Biomedical Optics*, Vol. 8, pp. 121–47, 02 2003.

83. Sharma, V., D. Kashyap, A. Mathker et al., “Optical reflectance spectroscopy for detection of human prostate cancer,” *Conference Proceedings : ... Annual International Conference of the IEEE Engineering in Medicine and Biology Society. IEEE Engineering in Medicine and Biology Society. Conference*, Vol. 2009, pp. 118–21, 09 2009.

84. Arifler, D., R. A Schwarz, S. K Chang, and R. Kortum, “Reflectance spectroscopy for diagnosis of epithelial precancer: Model-based analysis of fiber-optic probe designs to resolve spectral information from epithelium and stroma,” *Applied Optics*, Vol. 44, pp. 4291–305, 08 2005.

85. Sharma, V., D. Kashyap, A. Mathker et al., “Investigation of fiber-optic probe designs for optical spectroscopic diagnosis of epithelial pre-cancers,” *Lasers in Surgery and Medicine*, Vol. 34, pp. 25–38, 01 2004.

86. Joshua Pfefer, T., A. Agrawal, and R. A Drezek, “Oblique-incidence illumination and collection for depth-selective fluorescence spectroscopy,” *Journal of Biomedical Optics*, Vol. 10, p. 44016, 07 2005.

87. Wallace, M., A. Wax, D. N Roberts, and R. N Graf, “Reflectance spectroscopy,” *Gastrointestinal Endoscopy Clinics of North America*, Vol. 19, pp. 233–42, 05 2009.

88. Schelkanova, I., A. Pandya, A. Muhaseen, G. Saiko, and A. Douplik, “13 - early optical diagnosis of pressure ulcers,” in *Biophotonics for Medical Applications* (Meglinski, I., ed.), Woodhead Publishing Series in Biomaterials, pp. 347 – 375, Woodhead Publishing, 2015.

89. Sharma, M., E. Marple, and J. W. Tunnell, “Design and characterization of a novel multimodal fiber-optic probe and spectroscopy system for skin cancer applications,” *Rev Sci Instrum*, Vol. 85, 08 2014.

90. Garcia-Uribe, A., K. Chinna Balareddy, J. Zou, and L. V. Wang, “Micromachined fiber optical sensor for in vivo measurement of optical properties of human skin,” *Sensors Journal, IEEE*, Vol. 8, pp. 1698 – 1703, 11 2008.

91. Garcia-Uribe, A., J. Zou, M. Duvic, J. H. Cho-Vega, V. G. Prieto, and L. V. Wang, “In vivo diagnosis of melanoma and nonmelanoma skin cancer using oblique incidence diffuse reflectance spectrometry.,” *Cancer Research*, Vol. 72 11, pp. 2738–45, 2012.

92. Hamamatsu Inc., “Mini spectrometer, micro series, c12666ma,” 2019. Online; accessed February 15, 2019.

93. Thorlabs Inc., “Guide to connectorization and polishing optical fibers.” Online; accessed February 17, 2019.

94. Carnicom, C. E., “Morgellons : In the laboratory,” 2011. Online; accessed February 17, 2019.

95. Hennesy, R., Goth, W., Sharma, M. et al., “Effect of probe geometry and optical properties on the sampling depth for diffuse reflectance spectroscopy,” *Journal of Biomedical Optics*, Vol. 19, pp. 19 – 19 – 6, 2014.

96. Irving J. Bigio, S. F., *Quantitative Biomedical Optics: Theory, Methods, and Applications 1st Edition*, Cambridge Texts in Biomedical Engineering, 2016.

97. Lo, J., B. Yu, H. L Fu et al., “A strategy for quantitative spectral imaging of tissue absorption and scattering using light emitting diodes and photodiodes,” *Optics Express*, Vol. 17, pp. 1372–84, 03 2009.

98. Dhar, A., K. S. Johnson, M. Novelli et al., “Elastic scattering spectroscopy for the diagnosis of colonic lesions: Initial results of a novel optical biopsy technique,” *Gastrointestinal Endoscopy*, Vol. 63, pp. 257–61, 03 2006.

99. Kienle, A., L. Lilge, M. S. Patterson et al., “Spatially resolved absolute diffuse reflectance measurements for non-invasive determination of the optical scattering and absorption coefficients of biological tissue,” *Applied optics*, Vol. 35, pp. 2304–14, 05 1996.

100. Center for Devices and Radiological Health, “Electro-optical sensors for the in vivo detection of cervical cancer and its precursors: Submission guidance—not for implementation,” 1997. U.S. Food and Drug Administration.

101. Vo-Dinh, T., ed., *Biomedical Photonics Handbook, 3 Volume Set, 2nd Ed.*, North Caroline, USA: CRC Press, 2014.

102. Ocean Optics, “Bend radius and mechanical,” 2019. Available: https://oceanoptics.com/product-category/bend-radius-and-mechanical/.

103. Karamavuş, Y., and M. Özkan, “Newborn jaundice determination by reflectance spectroscopy using multiple polynomial regression, neural network, and support vector regression,” *Biomedical Signal Processing and Control*, Vol. 51, pp. 253 – 263, 2019.

104. Karamavuş, Y., and M. Özkan, “Determination of newborn jaundice level by transcutaneous bilirubin measurement,” in *2018 26th Signal Processing and Communications Applications Conference (SIU)*, pp. 1–4, May 2018.

105. Rajaram, N., T. H Nguyen, and J. W Tunnell, “Lookup table-based inverse model for determining optical properties of turbid media,” *Journal of Biomedical Optics*, Vol. 13, p. 050501, 09 2008.

106. W McMurdy, J., G. D Jay, S. Suner et al., “Diffuse reflectance spectra of the palpebral conjunctiva and its utility as a noninvasive indicator of total hemoglobin,” *Journal of Biomedical Optics*, Vol. 11, p. 014019, 01 2006.

107. Baty, F., C. Ritz, S. Charles (Bajard, M. Brutsche, J.-P. Flandrois, and M. Delignette-Muller, “A toolbox for nonlinear regression in r : The package nlstools,” *Journal of Statistical Software*, Vol. 66, pp. 1–21, 08 2015.

108. C. Nash, J., and R. Varadhan, “Unifying optimization algorithms to aid software system users: optimx for r,” *JSS Journal of Statistical Software August*, Vol. 43, 09 2011.

109. Kutner, M. H., J. Christopher,J.N. Nachtsheim et al., *Applied Linear Regression Models 4th ed.*, McGraw-Hill Irwin Series Operations and Decision Sciences, 2004.

110. Gatignon, H., *Statistical Analysis of Management Data, 2nd ed*, New York: Springer-Verlag, 2010.

111. Haykin, S., *Neural Networks: A Comprehensive Foundation (2nd Edition)*, Neural Networks, 2004.

112. Liu, W., Z. Wang, X. Liu et al., “A survey of deep neural network architectures and their applications,” *Neurocomputing*, Vol. 234, 12 2016.

113. Hinton, G., l. Deng, D. Yu et al., “Deep neural networks for acoustic modeling in speech recognition: The shared views of four research groups,” *Signal Processing Magazine, IEEE*, Vol. 29, pp. 82–97, 11 2012.

114. Han, K., D. Yu, and I. Tashev, “Speech emotion recognition using deep neural network and extreme learning machine,” 09 2014.

115. Krizhevsky, A., I. Sutskever, and G. E. Hinton, “Imagenet classification with deep convolutional neural networks,” *Neural Information Processing Systems*, Vol. 25, 01 2012.

116. Simonyan, K., and A. Zisserman, “Very deep convolutional networks for large-scale image recognition,” *ArXiv 1409.1556*, 09 2014.

117. Zhao, W., Z. Guan, L. Chen, X. He, D. Cai et al., “Weakly-supervised deep embedding for product review sentiment analysis,” *IEEE Transactions on Knowledge and Data Engineering*, Vol. PP, pp. 1–1, 09 2017.

118. Tao, D., C. Hong, J. Yu, J. Wan, and M. Wang, “Multimodal deep autoencoder for human pose recovery,” *IEEE Transactions on Image Processing : a Publication of the IEEE Signal Processing Society*, Vol. 24, 10 2015.

119. Hong, C., X. Chen, X. Wang, and C. Tang, “Hypergraph regularized autoencoder for image-based 3d human pose recovery,” *Signal Processing*, Vol. 124, 10 2015.

120. Holmstrom, L., and P. Koistinen, “Using additive noise in back-propagation training,” *IEEE Transactions on Neural Networks / a Publication of the IEEE Neural Networks Council*, Vol. 3, pp. 24–38, 02 1992.

121. Hak Lim, S., and M. M. Nojiri, “Spectral analysis of jet substructure with neural networks: boosted higgs case,” *Journal of High Energy Physics*, Vol. 2018, 10 2018.

122. M Balabin, R., and E. Lomakina-Rumyantseva, “Neural network approach to quantum-chemistry data: Accurate prediction of density functional theory energies,” *The Journal of Chemical Physics*, Vol. 131, p. 074104, 09 2009.

123. M. Balabin, R., R. Safieva, and E. Lomakina-Rumyantseva, “Wavelet neural network (wnn) approach for calibration model building based on gasoline near infrared (nir) spectra,” *Chemometrics and Intelligent Laboratory Systems*, Vol. 93, pp. 58–62, 08 2008.

124. Vapnik, V., *The Nature of Statistical Learning Theory, 1st ed*, New York: Springer Verlag, 2000.

125. Thissen, U., R. van Brakel, A. de Weijer et al., “Using support vector machines for time series prediction,” *Chemometrics and Intelligent Laboratory Systems*, Vol. 69, pp. 35–49, 11 2003.

126. Suykens, J., and J. Vandewalle, “Least squares support vector machine classifiers,” *Neural Processing Letters*, Vol. 9, pp. 293–300, 06 1999.

127. Scholkopf, B., A.J. Smola, *Learning with kernels: support vector machines, regularization, optimization, and beyond*, USA: MIT press, 2001.

128. N. Cristianini, J. S.-T., *An introduction to support vector machines and other kernel-based learning methods*, USA: Cambridge university press, 2000.

129. Nagar, G., B. Vandermeer, S. Campbell, and M. Kumar, “Reliability of transcutaneous bilirubin devices in preterm infants: A systematic review,” *Pediatrics*, Vol. 132, 10 2013.

130. Angelopoulo, E. *Technical Reports (CIS)*, pp. 584, title = The reflectance spectrum of human skin, 12 1999.

131. Bhutani, V. K., G. R. Gourley, S. Adler, et al., “Noninvasive measurement of total serum bilirubin in a multiracial predischarge newborn population to assess the risk of severe hyperbilirubinemia,” *Pediatrics*, Vol. 106, no. 2, pp. e17–e17, 2000.

132. Jacques, S., I. Saidi, A. Ladner, and D. Oelberg, “Developing an optical fiber reflectance spectrometer to monitor bilirubinemia in neonates,” in *Proceedings of SPIE - The International Society for Optical Engineering*, Vol. 2975, pp. 115–124, Society of Photo-Optical Instrumentation Engineers, 1997.

133. Shapiro, S. S., and M. B. Wilk, “An analysis of variance test for normality (complete samples),” *Biometrika*, Vol. 52, no. 3/4, pp. 591–611, 1965.

134. Kleinbaum, D. G., and L. L. Kuppe, *Applied Regression Analysis and Other Multivariable Methods*, USA: Cengage Learning, 2014.

135. Filliben, J., and W. F. Guthrie, “Nist sematech engineering statistics handbook. Online,” 2016. Available: https://www.nist.gov/programsprojects/nistsematech-engineering-statistics-handbook.

136. Bishop, C. M., *Neural networks for pattern recognition*, Oxford University Pres, 1st ed., 1995.

137. Chapelle, O., B. Schlkopf, and A. Zien, *Semi-Supervised Learning*, The MIT Press, 1st ed., 2010.

138. Chapelle, O., and V. Vapnik, “Model selection for support vector machines,” in *Proceedings of the 12th International Conference on Neural Information Processing Systems*, NIPS’99, (Cambridge, MA, USA), pp. 230–236, MIT Press, 1999.

139. Hill, T., *Model extremely complex functions, neural network*, Statsoft, 1st ed., 2016.

140. Cazon, A., T. Doredo, A. Lopez et al., “Determining the correlation and accuracy of three methods of measuring neonatal bilirubin concentration : Serum , capillary and transcutaneous bilirubin,” 2017.

141. L Porter, M., and B. L Dennis, “Hyperbilirubinemia in the term newborn,” *American Family Physician*, Vol. 65, pp. 599–606, 03 2002.

142. Romagnoli, C., E. Zecca, P. Catenazzi et al., “Transcutaneous bilirubin measurement: Comparison of respironics bilicheck and jm-103 in a normal newborn population,” *Clinical Biochemistry*, Vol. 45, pp. 659–62, 03 2012.

143. Panburana, J., S. Boonkasidach, and S. Rearkyai, “Accuracy of transcutaneous bilirubinometry compared to total serum bilirubin,” *Journal of the Medical Association of Thailand = Chotmaihet Thangphaet*, Vol. 93 Suppl 2, pp. S81–6, 02 2010.

144. Badiee, Z., M. Mohammadizadeh, and M. Shamee, “Diagnostic usefulness of transcutaneous bilirubinometry in very preterm newborns,” *International Journal of Preventive Medicine*, Vol. 3, pp. 262–5, 04 2012.

145. Raimondi, F., S. Lama, F. Landolfo et al., “Measuring transcutaneous bilirubin: a comparative analysis of three devices on multiracial population,” *BMC Pediatrics*, Vol. 12, p. 70, 06 2012.

146. Grohmann, K., M. Roser, B. Rolinski, I. Kadow, C. Müller, A. Goerlach-Graw, M. Nauck, and H. Küster, “Bilirubin measurement for neonates: Comparison of 9 frequently used methods,” *Pediatrics*, Vol. 117, pp. 1174–83, 05 2006.

147. Turkmen, K., M. Aydogdu, and S. Gokbulut, “Transcutaneous measurement of bilirubin in turkish newborns: comparison with total serum bilirubin,” *The Turkish Journal of Pediatrics*, Vol. 53, pp. 67–74, 01 2011.

148. Nanjundaswamy, S., A. Petrova, R. Mehta, and T. Hegyi, “Transcutaneous bilirubinometry in preterm infants receiving phototherapy,” *American Journal of Perinatology*, Vol. 22, pp. 127–31, 04 2005.

149. Gen Consultin, “Global jaundice meter market outlook 2017-2022,” Tech. Rep. WGR3325212, Gen Consulting, 2018 April.